Universidad de Granada

FACULTY OF SCIENCE

DEPARTMENT OF APPLIED PHYSICS

MASTER THESIS:

CLIMATE CHANGE PROJECTIONS FOR WINTER STREAMFLOW IN DOURO RIVER

Rubén Cruz García

Supervised by:
María Jesús Esteban Parra
Sonia Raquel Gámiz Fortís

2014/2015

Contents

Abstract

In the last decades, the interest in the projections of future climate and its impacts on water resources have grown as a means to identify appropriate mitigation and adaptation strategies, for example in reference to hydrological and agricultural activities. Motivated by this reason, in this work climate change projections for the winter streamflow of the Douro River have been obtained, for the period 2071-2099, using the Principal Component Regression (PCR) method.

The winter streamflow time series (January to March averaged) from eight stations distributed over the basin, covering the period 1950-2011, were used as predictand variables, while the principal components (PCs) of the anomalies of the sea level pressure (SLP) in winter (December to February averaged) were used as predictors of the streamflow for the development of a statistical downscaling model. The period 1950-1995 was used for calibration the regression model, while 1996-2011 was used for validation. In general, the correlation coefficients between the observed and predicted values are around 0.75, being the highest errors the estimations of the maximum peak flows.

Finally, the statistical downscaling model obtained from the observational SLP data was applied to the SLP data from the outputs of the Global Circulation Models (GCMs) MIROC5, CESM1 and IPSL-CM5A-MR, for the period 2071-2099, under the climate change scenarios RCP2.6, RCP4.5 and RCP8.5. The main result is a generalized projected decrease in the winter streamflow of the Douro River for all models and scenarios.

Resumen

En las últimas décadas, el interés en las proyecciones del clima futuro y sus impactos en los recursos hídricos ha crecido como medio para identificar estrategias de mitigación y adaptación adecuadas, por ejemplo, en lo concerniente a las actividades hidrológicas y agrícolas. Motivados por esta razón, en este trabajo se han obtenido proyecciones de cambio climático del caudal de invierno del río Duero, para el período 2071-2099, utilizando el método de Regresión de Componentes Principales (PCR).

Las series temporales del caudal de invierno (promedio de enero a marzo) de ocho estaciones distribuidas a lo largo de la cuenca, en el período 1950-2011, se han utilizado como variables a predecir, mientras que las componentes principales (PCs) de las anomalías de la presión a nivel del mar (SLP) en invierno (promedio de diciembre a febrero) se utilizaron como predictores del caudal para el desarrollo de un modelo de *downscaling* estadístico. El período 1950-1995 se utilizó para la calibración del modelo de regresión, mientras que 1996-2011 se utilizó para la validación. En general, los coeficientes de correlación entre los valores observados y los predichos son alrededor de 0.75, siendo los errores más altos debidos a las estimaciones de los picos de caudal máximo.

Por último, se ha aplicado el modelo de *downscaling* estadístico obtenido a partir de los datos observacionales de la SLP a los datos de SLP procedentes de las salidas de los modelos de circulación general (GCMs) MIROC5, CESM1 y IPSL-CM5A-MR, para el período 2071-2099, bajo los escenarios de cambio climático RCP2.6, RCP4.5 y RCP8.5. El principal resultado obtenido es una disminución generalizada del caudal de invierno del río Duero para todos los modelos y escenarios.

True science teaches, above all, to doubt and to be ignorant.

—***Miguel de Unamuno***—

La verdadera ciencia enseña, sobre todo, a dudar y a ser ignorante.

—***Miguel de Unamuno***—

Chapter 1

Introduction

1.1 Climate change

Climate can be defined as the synthesis of a fluctuating set of weather conditions, in a certain area, corresponding to a time period long enough to be geographically representative (Tullot, 2000), ranging from months to thousands or millions of years. While climate change refers to a change in the state of the climate that can be identified (e.g., by using statistical tests) by changes in the mean and/or the variability of its properties, and that persists for an extended period, typically decades or longer (IPCC, 2013).

We can consider the climate system as a combination of an undetermined level of internal variability or noise due to the inherent chaotic nature of the system, superimposed on the net effect of a number of external forcings (Gómez-Navarro et al., 2010). Hence, when creating reconstructions of the past or simulations of future, the attribution of observed trends to the anthropogenic forcing could be often spoiled by this variability.

Radiative forcing (RF) is the net change in the energy balance of the Earth system due to some perturbation, and the anthropogenic forcing is human-induced forcing. It is usually expressed in watts per square meter ($\mathrm{W}m^{-2}$) averaged over a certain period of time and quantifies the energetic imbalance that occurs when the brought change takes place. Although generally it is difficult to observe, calculated RF provides a simple quantitative basis for comparing some aspects of the potential climate response to different imposed agents, especially global mean temperature, and therefore it is widely used in the scientific community (IPCC, 2013).

The current climate change is a reality, which can be demonstrated by a series of indicators, which include physical responses such as changes in the surface temperature or the sea level. Also, according to the Intergovernmental Panel on Climate Change (IPCC) Fifth Assessment Report (AR5), climate change can lead to other effects on the Earth's physical system that are also indicators of climate change, such as the ocean acidification or the sea ice loss. Some key examples of such changes in important climate parameters are:

- Greenhouse gas (GHG) concentrations: The modification of the concentration of GHGs in the atmosphere due to the human activities is an example of an anthropogenic forcing. However, it can also be caused by the volcanic forcing, whose eruptions can inject large amounts of SO_2 gas in the stratosphere (Textor et al., 2003). The GHG emissions are the first element in the causal chain of climate change and thus those factors that directly affect the GHG emissions can be regarded as prime drivers of global warming (Argüeso Barriga, 2011).

- Surface temperatures: Global average temperatures have been rising for the past half-century, and the trend has accelerated in recent decades (IPCC, 2007).

- Extreme events: At present, single extreme events cannot generally be directly attributed to anthropogenic influence, although the change in likelihood for the event to occur has been determined for some events by accounting for observed changes in climate (IPCC, 2013).

1.2 Climate scenarios

The measuring of the emissions and the climate scenarios are a central component for performing the developing of the climate change projections, because as we already know global warming is due largely to the increase in greenhouse gases in the atmosphere. The scenarios were designed to span a broad range of plausible futures, but are not aimed at predicting the most likely outcome (IPCC, 2013).

In the Third Assessment Report (TAR) and Fourth Assessment Report (AR4) of the IPCC, the emission scenarios are known as SRES scenarios, since they were published in the IPCC Special Report on Emissions Scenarios (Nakicenovic et al., 2000). There are 40 different SRES scenarios proposed by the IPCC. The set of scenarios consists of six scenario groups drawn from the four families: one group each in A2, B1, B2, and three groups within the A1 family, characterizing alternative developments of energy technologies: A1FI (fossil fuel intensive), A1B (balanced), and A1T (predominantly non-fossil fuel).

Scenario uncertainty refers to the uncertainties that arise due to limitations in our understanding of future emissions, concentrations or forcing trajectories. Scenarios help in the assessment of future developments in complex systems that are either inherently unpredictable, or that have high scientific uncertainties (IPCC, 2001). The societal choices defining future climate drivers are surrounded by considerable uncertainty, and these are explored by examining the climate response to a wide range of possible futures. As we commented before, in past reports, emissions scenarios from the SRES were used as the main way of exploring uncertainty in future anthropogenic climate drivers, but since the AR5 new scenarios of future forcings have been developed to replace the SRES, using Integrated Assessment Models (IAMs). These scenarios, named Representative Concentration Pathways (RCPs),

include four new scenarios designed to explore a wide range of future climate characterized by representative trajectories of well-mixed greenhouse gas (WMGHG) concentrations and other anthropogenic forcing agents, but they also provide gas emissions.

The RCPs scenarios are referred to as pathways in order to emphasize that they are not definitive scenarios, but rather internally consistent sets of time-dependent forcing projections that could potentially be realized with more than one underlying socioeconomic scenario. It must be noted that SRES scenarios assumed that no climate mitigation policy would be undertaken, unlike the RCP scenarios. RCPs scenarios are identified by the approximate value of the RF (in $\mathrm{W}m^{-2}$) at 2100 or at stabilization after 2100 in their extensions, relative to pre-industrial (Meinshausen et al., 2011b; Moss et al., 2008).

According to Wayne (2013) the main characteristics of each of the RCPs scenarios are:

- RCP8.5 was developed using the Model for Energy Supply Systems And their General Environmental impact (MESSAGE) model and the IIASA Integrated Assessment Framework by the International Institute for Applied Systems Analysis (IIASA), Austria. This RCP is characterized by increasing greenhouse gas emissions over time, representative of scenarios in the literature that lead to high greenhouse gas concentration levels (Riahi et al., 2007). This RCP combines the assumption about high population and relatively slow income growth with modest rates of technological change and energy intensity improvements, leading high energy demand and GHG emissions in absence of climate change policies.

- RCP6 was developed by the Asia-Pacific Integrated Model (AIM) modeling team at the National Institute for Environmental Studies (NIES) in Japan. It is a stabilization scenario in which total RF is stabilized shortly after 2100, without overshoot, by the application of a range of technologies and strategies for reducing greenhouse gas emissions (Fujino et al., 2006; Hijioka et al., 2008).

- RCP4.5 was developed by the Global Change Assessment Model (GCAM) modeling team at the Pacific Northwest National Laboratory's Joint Global Change Research Institute (JGCRI) in the United States. It is a stabilization scenario in which total RF is stabilized shortly after 2100, without overshooting the long-run radiative forcing target level (Clarke et al., 2007; Smith and Wigley, 2006; Wise et al., 2009).

- RCP2.6 was developed by the Integrated Model to Assess the Global Environment (IMAGE) modeling team of the PBL Netherlands Environmental Assessment Agency. The emission pathway is representative of scenarios in the literature that lead to very low greenhouse gas concentration levels. It is a "peak-and-decline" scenario; its RF level first reaches a value of around 3.1 $\mathrm{W}m^{-2}$ by mid-century, and returns to 2.6 $\mathrm{W}m^{-2}$ by 2100. In order to

reach such RF levels, greenhouse gas emissions (and indirectly emissions of air pollutants) are substantially reduced, over time (Van Vuuren et al., 2007).

In broad terms, the low-emission scenario RCP2.6 is similar to the SRES B1 scenario, RCP4.5 is similar to A1B, RCP6 is similar to A1FI, and RCP8.5 is a new high-emission scenario (Evans and McGregor, 2012). The time evolution of all of these scenarios can be seen in Figure 1.1. The RF of RCP2.6 is hence lower by 1.9 Wm^{-2} than the three SRES scenarios (Johns et al., 2011). RCP4.5 and SRES B1 have similar RF at 2100, and comparable time evolution (within 0.2 Wm^{-2}). The RF of SRES A2 is lower than RCP8.5 throughout the 21st century, mainly due to a faster decline in the radiative effect of aerosols in RCP8.5 than SRES A2, but they converge to within 0.1 Wm^{-2} at 2100. RCP6.0 lies in between SRES B1 and SRES A1B.

RCP2.6, which assumes strong mitigation action, yields a smaller temperature increase than any SRES scenario. The temperature increase with the RCP4.5 and SRES B1 scenarios are close and the temperature increase is larger with RCP8.5 than with SRES A2. The spread of projected global mean temperature for the RCP scenarios is considerably larger (at both the high and low response ends) than for the three SRES scenarios used in CMIP3 (B1, A1B and A2) as a direct consequence of the larger range of RF across the RCP scenarios compared to that across the three SRES scenarios (IPCC, 2013).

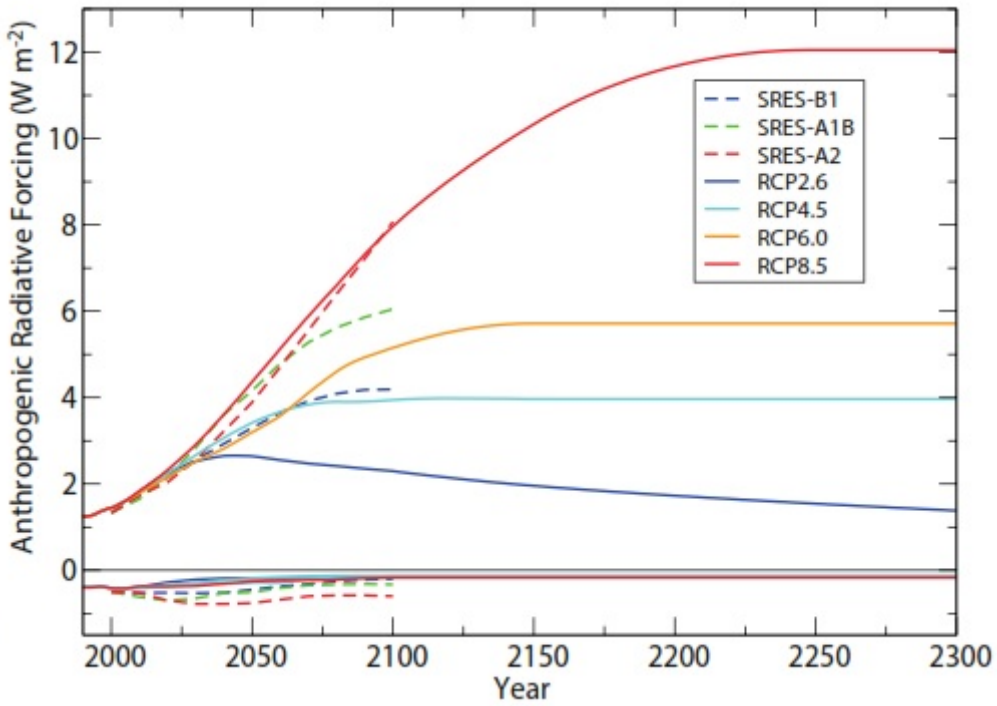

Figure 1.1 – Time evolution of the total anthropogenic (positive) and anthropogenic aerosol (negative) radiative forcing (RF) relative to pre-industrial (about 1765) between 2000 and 2300 for RCP scenarios and their extensions (continuous lines), and SRES scenarios (dashed lines) as computed by the Integrated Assessment Models (IAMs) used to develop those scenarios. The four RCP scenarios used in CMIP5 are: RCP2.6 (dark blue), RCP4.5 (light blue), RCP6.0 (orange) and RCP8.5 (red). The three SRES scenarios used in CMIP3 are: B1 (blue, dashed), A1B (green, dashed) and A2 (red, dashed). Positive values correspond to the total anthropogenic RF. Negative values correspond to the forcing from all anthropogenic aerosol–radiation interactions (i.e., direct effects only). The total RF of the SRES and RCP families of scenarios differs in 2000 because the number of forcings represented and our knowledge about them have changed since the TAR. The total RF of the RCP family is computed taking into account the efficacy of the various forcings (Source: Meinshausen et al., 2011a, cited by the IPCC (2013)).

1.3 Climate models and downscaling

Climate models are extremely sophisticated computer programs that encapsulate our understanding of the climate system and try to numerically simulate the complex interactions between the atmosphere, ocean, land surface, snow and ice, the global ecosystem and a variety of chemical and biological processes for making climate predictions, projections of future climate or for investigating the response of the climate system to various forcings, by combining a large set of well-established physical laws (IPCC, 2013). They are essential in climate science due to the impossibility to carry out controlled experiments in the real climate increasing the CO_2 within the Earth's atmosphere and obtain the results hundred years later taking measures to test the anthropogenic warming hypothesis.

Climate models of today are better than their predecessors. The rising computational power since the IPCC First Assessment Report in 1990 has made possible the use of models of increasing complexity. However, every bit of added complexity also introduces new sources of possible error. Furthermore, despite the progress that has been made, scientific uncertainty regarding the details of many processes remains (IPCC, 2013).

There are different types of climate models, the Global Circulation Models (GCMs) and the Regional Circulation Models (RCMs). A GCM consists of the coupling of several submodels, including at least a complete atmospheric model and an ocean model. For this the reason they are usually called Atmosphere–Ocean General Circulation Models (AOGCMs). Each of these models simulates the globe as a whole, and they are coupled in the sense that they run simultaneously and exchange energy, matter and momentum. However, they require a huge computational cost due to the many submodels included and the large number of grid points where these models have to be solved iteratively to cover the whole planet (Gómez Navarro, 2011).

The other important type of climate models are the regional climate models (RCMs). The RCMs are applied over a limited-area domain with boundary conditions either from global reanalyses or GCM outputs. RCMs are able to capture many of the regional-scale phenomena that the GCMs are unable to resolve. According to Rummukainen (2010) their resolution has increased and new components have been added to the climate system, developing their process descriptions as well.

The importance of this last type of models lies in their high resolution. Although we could obtain regional climate information directly from global models, we would encounter the problem of horizontal resolution, which would not allow us to resolve features that are important at regional scales. For this reason, strategies that are based on the global simulation data and which add them a greater detail are used. These techniques are called downscaling.

There are two main approaches to downscaling: statistical and dynamical. The former uses statistical models establishing a mathematical relationship between a large-scale circulation field with the evolution of variables at a local scale (Evans and McGregor, 2012). These statistical models need to be calibrated in a control period,

after which they can be used to predict the local variables using the large scale field as predictor. They are computationally cheaper, allowing to work with different models and scenarios. However, their main disadvantage is that they assume that the relations established between predictand and predictor in the calibration period hold on for past or future periods of time (Wilby et al., 1998; Zorita and Von Storch, 1999). On the other hand, dynamical downscaling lies in solving the equations of the atmosphere using a physical model at higher resolutions than the GCM, that is, using a RCM focused in a limited area domain but imposing some restrictions (Argüeso Barriga, 2011).

1.4 Impact of the Climate Change on Hydrology

Climate change has a direct and important impact on water resources. The effects on these resources will manifest not only in the variation of the quantity but also in the alteration of the quality and temporal distribution (Moreno et al., 2005). A good example given by the IPCC (2013) could be an earlier spring melt, altering the timing of peak springtime flow in rivers receiving snowmelt, and therefore producing a decrease on the later flow rates, which could affect the water resource management. According to Rasilla et al. (2013), it will certainly become a great challenge to be faced by humankind. That is the reason why the scientific community must provide a reliable evaluation of the current status of the water resources at regional and local scales, and to predict their future response to the climate changes due to global warming.

Although the flow and storage of water in the Earth's climate system are highly variable, it is clear that other changes apart from those due to natural variability are expected by the end of the current century (IPCC, 2013). The extent to which climate change affects water resources is evaluated through the changes observed in the different variables (González-Zeas et al., 2010). The best example could be the proved increase in temperatures (Dasari et al., 2014), what will cause a net increase in rainfall, surface evaporation and sea level (Chang et al., 2015). Those changes are governed by the amount of energy that global warming adds to the climate system (IPCC, 2013).

A warmer atmosphere can have more water vapour and it can thereby induce greater evapotranspiration (evaporation and transpiration from plants). However, the increase of carbon dioxide in the atmosphere reduces the plant's tendency to transpire, partly counteracting the effect of warming (IPCC, 2013).

Figure 1.2 shows a schematic diagram of projected changes for the water cycle. As we can see, the boundaries of high or low moisture regions may change. A further complicating factor is the character of rainfall. Projections show that precipitation events overall will tend to occur less frequently, but the events with an extreme nature could occur every less time, that is, more floods, but yet longer dry periods between rain events (IPCC, 2013).

We must not confuse hydric contribution and water resources. Hydric contri-

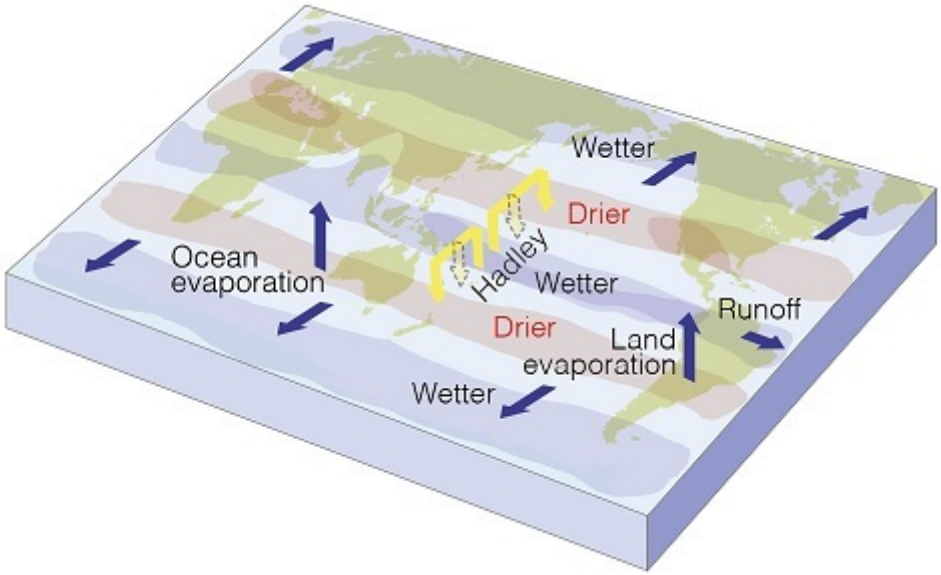

Figure 1.2 – Schematic diagram of projected changes in major components of the water cycle. The blue arrows indicate major types of water movement changes through the Earth's climate system: poleward water transport by extratropical winds, evaporation from the surface and runoff from the land to the oceans. The shaded regions denote areas more likely to become drier or wetter. Yellow arrows indicate an important atmospheric circulation change by the Hadley Circulation, whose upward motion promotes tropical rainfall, while suppressing subtropical rainfall. Model projections indicate that the Hadley Circulation will shift its downward branch poleward in both the Northern and Southern Hemispheres, with associated drying. Wetter conditions are projected at high latitudes, because a warmer atmosphere will allow greater precipitation, with greater movement of water into these regions (Source: IPCC, 2013).

bution, defined as the total volume of water annually count at a point in the river basin in natural regime, is initially conditioned by precipitation, temperature, use and land cover and soil and subsoil characteristics (Moreno et al., 2005); while water resources is defined as the available resources or potentially available in sufficient quantity and quality, at a place and at an appropriate time to satisfy an identifiable demand (WMO, 2012), and is the second term with which we must deal, as its management presents a high degree of uncertainty, and the demand is the main problem, which depends not only on climate but also of technical and socioeconomic changes.

Spain is a country with a huge variety of water uses. Mainly its developed agriculture and its high hydroelectric potential have led to the development of a large amount of reservoirs, dams and underground water intakes (Moreno et al., 2005). And it is, by far, the agricultural activity the largest water consumer, representing on average 40% of the total water consumption in Europe, although in Mediterranean countries, like Spain, it represents 60–80% (Rasilla et al., 2013).

Unfortunately, Spanish water resources have a high spatiotemporal irregularity in natural regime, especially when it is compared with the European average. For this reason, it has been necessary a marked human intervention in the hydrologi-

cal cycle throughout the time, having profoundly altered its natural characteristics (Garrote de Marcos et al., 2008).

According to Falkenmark et al. (1976) a consumption of 20% of the total renewable water resources is considered as the limit of overexploitation of a system. In most of the basins of Spain water resources are overused. As shown in the Water White Book in Spain (MIMAM, 1998), the Douro River is dangerously in the limit of overexploitation, with 14175 Hm^3 of input and 2929 Hm^3 of intake, which makes a relationship of 21% of consumption. Meanwhile, other important rivers in Spain such as the Tagus, the Ebro or the Guadalquivir have an exploitative relationship of 20%, 29% and 29%, respectively. A notable case is the Segura River with 96% of consumption.

Therefore, natural water resources in the Iberian Peninsula (IP) are used intensively, especially in agriculture, but also in other sectors, such as hydropower industry or tourism. Together with the increase in water demand, the observed decrease in water availability has intensified the situation of water stress in the IP. A country of this nature is very sensitive to declines that may present the inherent water resources to climate change, and, as mentioned before, adapting to the coming water stress conditions will demand economic, social and technical measures beyond the frontiers of each country. Thus, economic development and environmental protection must go together to avoid unintended effects in the near future (Duarte et al., 2014).

1.5 Teleconnection patterns

Teleconnections are integral phenomena of the climate system, which indicate recurring fluctuations in the circulation (atmospheric or oceanic) in distant areas correlated with each other (Kawale et al., 2011). Therefore, they contribute to climate variability (at regional level) of precipitation, temperature and some ecosystems. Teleconnections reflect important aspects of internal variability of the system and the interaction between the atmosphere and other components of greater inertia as oceans. These are determined by a spatial structure or teleconnection pattern (TCP) and a temporal series (or teleconnection index) which characterizes its evolution through the time, its amplitude and its phase. A challenge of great interest for climate research is the pursuit of teleconnection signals which allow explaining the occurrence of anomalous weather events such as droughts, floods and thermal extremes, as well as improving climate predictions (Pérez et al., 2010). Here, the most important pattern affected the IP are presented.

North Atlantic Oscillation (NAO)

One of the most prominent teleconnection patterns in all seasons, and the predominant in the North Atlantic sector (including the IP) is the North Atlantic Oscillation (NAO). The NAO consists of a north–south pressure dipole of geopotential

anomalies, with one center located over Greenland and the other center, of opposite sign, spanning between 35°N and 40°N in the central North Atlantic (Hurrell, 1995).

According to Pérez et al. (2010), NAO justifies an important part of the precipitation variability in Europe, so that a positive phase of this oscillation, characterized by an increase in pressure at the center of subtropical high pressures (in the Azores High), and a decrease over the center of subpolar low pressures (in the Icelandic Low), is associated with an increase in precipitation in northern Europe and a decrease in the European southwest; the opposite occurs for negative phase. This link with precipitation is explained by the close relationship between the NAO and the displacements of the zonal flow and the jet stream (Hurrell, 1995). In the positive phase air masses are from the northwest, dry and cold; while in the negative phase are from the southwest, hot and humid (Rodríguez-Puebla and Nieto, 2010).

The NAO index is obtained by projecting the NAO loading pattern, chosen as the first mode of a Rotated Empirical Orthogonal Function (EOF) analysis using monthly mean 500 mb height anomaly data, to the daily anomaly 500 mb height field over 0-90°N (NOAA).

As stated by Rodríguez-Puebla et al. (1998), the structure of the NAO experiences seasonal, interannual, decadal and multidecadal variations, exhibiting sometimes a tendency to remain in one phase for intervals which may last several years (Pérez et al., 2010).

There is a proved increase in the NAO index over the past few decades, and it is linked to the winter frequency of the "pure anticyclone" weather type described by Jenkinson and Collison (1977), which has grown significantly between 1948 and 2008 (Fernandez-Gonzalez et al., 2012). They also found positive correlations between the frequency of the cyclonic weather type and precipitation in many parts of the IP. To show this result, Figure 1.3a shows the time series of observed precipitation averaged over the IP in mm/day, and the NAO index from the Climate Prediction Center (NOAA) for winter (DJFM) season. In addition to the year to year fluctuations, the figure indicates a decrease in the linear trends in the case of precipitation and an increase in the case of the NAO index.

Additionally, there is a relation between precipitation variability and the NAO (Figure 1.3), which could be directly reflected in the seasonal flow of rivers, as there is a temporal lag based on the premise that a delay occurs between precipitation and runoff derived from physical processes such as snowmelt, interception, infiltration or the retention of flows in dams for hydropower generation (Trigo et al., 2004). NAO teleconnection pattern is especially high correlated in the IP and particularly in winter (Lorenzo-Lacruz et al., 2011; Rodríguez-Puebla and Nieto, 2010). Figure 1.3b indicates that precipitation in the western part of the IP is well linked to the NAO with the opposite sign (Rodríguez-Puebla and Nieto, 2010).

As commented in the Section 1.4, it is very difficult to carry out a properly water management in the IP because of the great variability of seasonal and annual flows, caused by the high spatio-temporal variability of precipitation (Esteban-Parra et al., 1998). Due to its importance, a lot of authors have tried to predict precipitation using the values of the NAO index (e.g Castro et al., 2011). Fernandez-Gonzalez

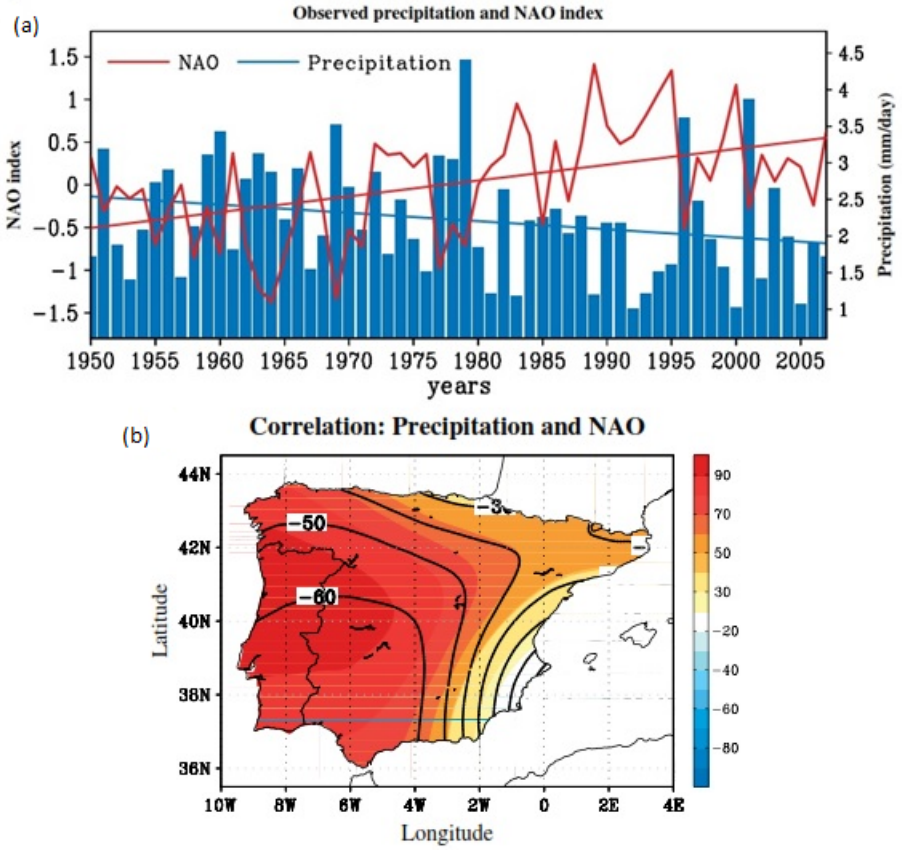

Figure 1.3 – **a.** Time series (in bars) and linear trend (blue line) of precipitation averaged over the Iberian Peninsula and NAO index (red line) for DJFM season. **b.** Correlation of precipitation and NAO index (multiplied by 100 in contour lines), leading EOF of precipitation (multiplied by 100 in shaded for DJFM) (Source: Rodríguez-Puebla and Nieto, 2010).

et al. (2012) indicated that if we could forecast the value of the NAO index for a winter some months before, then we would be able to obtain an accurate estimate of the amount of precipitation that would be recorded in that winter, providing large potential economic advantages (Trigo et al., 2004). However, Lorenzo-Lacruz et al. (2011) states that there is a non-stationary relationship between climate and the NAO, which must be better understood in order to advance in predicting available water resources in particular basins.

At the moment, climate projections for the XXI century show a trend toward the positive phase of the NAO, which would entail a reduction in the peninsular precipitation, especially in the southern half, and an overall temperature increase in the IP, with higher values the higher the concentration of greenhouse gases (Rodríguez-Puebla et al., 1998).

East Atlantic pattern (EA)

The East Atlantic (EA) pattern is the second prominent mode of low-frequency

variability over the North Atlantic, and appears as a leading mode in all months. The EA pattern is structurally similar to the NAO, and consists of a north-south dipole of anomaly centres which span the entire North Atlantic Ocean. The anomaly centres are displaced towards the southeast with respect to the NAO. However, the lower-latitude center contains a strong subtropical link in association with modulations in the subtropical ridge intensity and location. This subtropical link makes the EA pattern distinct from its NAO counterpart.

The positive phase of the EA pattern is associated with above-average surface temperatures in Europe in all months, and with below-average temperatures over the southern U.S. during January-May and in the north-central U.S. during July-October. It is also associated with above-average precipitation over northern Europe and Scandinavia, and with below-average precipitation across southern Europe.

East Atlantic-Western Russia pattern (EA-WR)

The EA-WR pattern consists of two main anomaly centres, located over the Caspian Sea and western Europe in winter. The patterns change in spring and autumn.

The main surface temperature anomalies associated with the positive phase of the EA-WR pattern reflect above-average temperatures over eastern Asia, and below-average temperatures over large portions of western Russia and northeastern Africa. The main precipitation departures reflect generally above-average precipitation in eastern China and below-average precipitation across central Europe.

Scandinavian pattern (SCAND)

The SCAND consists of a high pressure center over Scandinavia, with weaker centers of opposite sign over western Europe and eastern Russia / western Mongolia. The positive phase of this pattern is associated with positive height anomalies, sometimes reflecting major blocking anticyclones, over Scandinavia and western Russia, while the negative phase of the pattern is associated with negative height anomalies in these regions.

The positive phase of the Scandinavia pattern is associated with below-average temperatures across central Russia and also over western Europe. It is also associated with above-average precipitation across central and southern Europe, and below-average precipitation across Scandinavia.

1.6 Objectives

In view of the above, the main objective of this work is to obtain climate change projections of the Douro River winter streamflow for the period 2071-2099.

On the other hand, we also set some secondary objectives:

- To analyze the existence of the relationships between different teleconnection

patterns and the Douro winter streamflow.

- To evaluate the capacity of the sea level pressure (SLP) variability in the North Atlantic region at predicting the streamflow of an Iberian river.

- To evaluate the performance of three GCMs (MIROC5, CESM1 and IPSL-CM5A-MR) of the IPCC-AR5 at simulating the SLP in the North Atlantic region.

- To fit downscaling models to simulate the winter streamflow of the Douro River for the historic period (1951-2005), and consequently obtaining their bias in reference to that variable.

- To evaluate the skill of the downscaling models for the winter streamflow in the Douro River.

Chapter 2

Data

In this Master Thesis we will focus on the IP and more specifically on the Douro river basin, as it is an interesting area of study due to its climatic heterogeneity.

The IP encompasses 583254 km^2 and is located in a climatic transition zone between temperate and tropical latitudes. The existence of semidesertic, Mediterranean, Atlantic and high mountain environments leads to significant spatial variations in temperature and precipitation to which a large interannual variability is added.

The Douro River has the largest drainage basin (Figure 2.1) within the IP with an area of 97290 Km^2, which is also the highest of the great basins. Moreover, with 897 km in length it corresponds to one of the longest rivers in Iberia (second only to Tagus), running from the Iberian Mountains in north-eastern Spain down to the Atlantic Ocean across Portugal. There is a lack of proportionality between area, runoff and volume in the two countries due to the fact that the Douro Basin is a complex region from both the topographical and meteorological perspectives. This region includes prominent mountains, several mountain ranges, hilly areas, valleys and tributary streams.

The streamflow data base used in this work has been provided by the Center for Studies and Experimentation of Public Works, CEDEX. Time series from gauging stations and reservoirs with less than 5% of missing data in the period 1950-2011 have been considered. So, we have selected just eight stations whose gaps were filled by regression with well correlated neighboring stations. Table 2.1 shows a brief summary of the selected stations, while their localizations can be found in Figure 2.2.

The study of river flow regimes in the Iberian region using the calendar year (January to December) may result in misleading results, since the high winter precipitation would be splitted between two different years. Thus, it is usual to adopt the October-to-September definition of the hydrological year: the average river flow for the year 1961, say, is the sum of monthly flow from October 1960 until September 1961. We also have to remember the temporal lag commented in the Section 1.5, knowing that there is a delay between precipitation and runoff. For this reason we consider that the winter streamflow is given by the January-February-March (JFM)

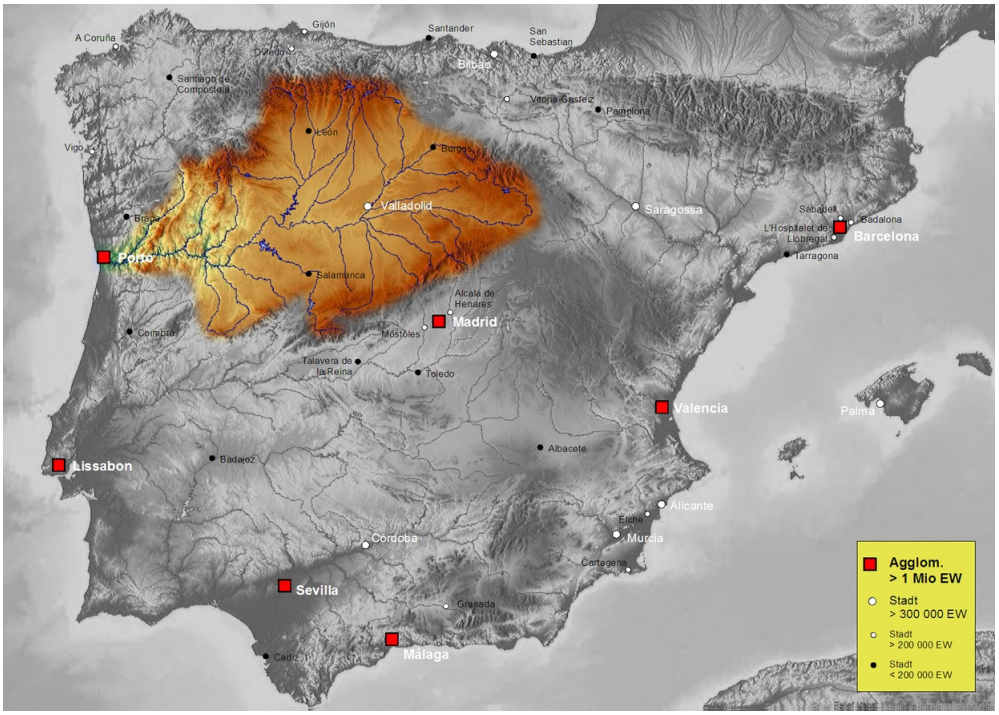

Figure 2.1 – Location of the international Douro river basin in the Iberian Peninsula and the catchments boundaries (Source: http://es.wikipedia.org/wiki/Cuenca_hidrogr%C3%A1fica_del_Duero)

averaged flow as is also sugared by Trigo et al. (2004).

In the present study, as predictor variable for winter Douro streamflow we use the sea level pressure (SLP) averaged from December to February (DJF), because the links between precipitation and atmospheric circulation tend to be the strongest in winter. Database used is the SLP monthly mean from the reanalysis data of the National Centers for Environmental Prediction-National Center for Atmospheric Research (NCEP-NCAR). This SLP data set has a temporal coverage from 1950 to 2011, and horizontal resolution of 2.5° X 2.5°.

Also, the SLP outputs from three GCMs of the CMIP5 for a historic (1951-2005) and a future period (2071-2099) are used. The GCMs are the following:

- CESM1 (CAM5): The Community Earth System Model (CESM) version 1 from the Community Atmosphere Model (CAM) version 5.0 is a coupled climate model composed of four separate models, simultaneously simulating the Earth's atmosphere, ocean, land surface and sea-ice, and one central coupler component. Equilibrium climate sensitivity of CESM1 is 4.10°C, which is higher than its predecessor.

- IPSL-CM5A-MR: It is the mid resolution version of the IPSL-CM5A Earth system model, from the Institut Pierre Simon Laplace (IPSL). The resolution is 1.25° x 2.5°, with 39 vertical levels for the atmosphere (144 x 143 L39) and

Name	Number	Type of station	UTM Coordinates (X,Y)	Average annual streamflow (m^3/s)
Covarrubias	2030	Natural watercourse	458015,4656096	12.751
Peral de Arlanza	2031	Natural watercourse	411343,4659287	15,139
Quintana del Puente	2036	Natural watercourse	397462,4656950	27,703
Toro	2062	Natural watercourse	298767,4598960	111,454
Morales del Rey	2082	Canalisation with shallow water channel	271646,4660092	6,148
Villalcampo	2002	Reservoir	743376,4597622	776820000
Castro	2003	Reservoir	734588,4606683	780120000
Ricobayo	2029	Reservoir	251040,4601807	408220000

Table 2.1 – Basic characteristics of the gauging stations and reservoir which have been chosen for this work. The average annual streamflow was obtained from CEDEX.

about 2°, with a meridional increased resolution of 0.5° near the Equator and with 31 vertical levels for the ocean (149 x 182 L31).

- MIROC5: The Model for Interdisciplinary Research on Climate (MIROC) version 5 was developed jointly at the Center for Climate System Research (CCSR), University of Tokyo; National Institute for Environmental Studies (NIES); and Japan Agency for Marine-Earth Science and Technology. It has the standard resolution of the T85 atmosphere and 18 ocean models.

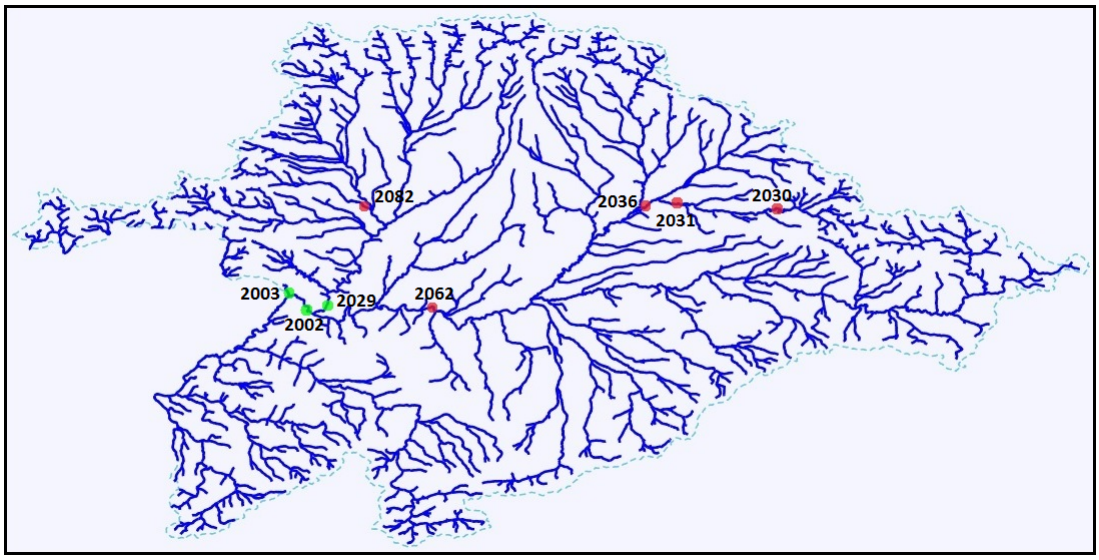

Figure 2.2 – Localization of the streamflow series analyzed in this work within the Spanish part of the Douro basin. Gauging stations are shown in red and reservoirs in green.

All SLP data, reanalysis and GCMs, were chosen for a range covering the area of latitude from 20° N to 90° N and longitude from 110° O to 70° E. But note that due to the different spatial resolution of the SLP outputs from the GCMs, we had to regrid all of them in order to have the same grid than the NCEP reanalysis data.

For computing the climate change projections of winter Douro streamflow, the RCPs scenarios 2.6, 4.5 and 8.5 have been chosen.

Finally, the monthly time series of the NAO, EA, EA-WR and SCAND teleconnection indices were obtained from the Climate Prediction Center (CPC) at the National Center of Environmental Predictions (NCEP; www.cpc.noaa.gov), and winter indices were computed using December-January-February average.

Chapter 3

Methodology

This section shows the methodology used in this work for computing climate change projections of Douro streamflow through statistical downscaling. There are many different statistical techniques that have been applied in order to downscale climate data. In this work we follow the methodological scheme based on the Principal Component Regression (PCR), developed by Palomino-Lemus et al. (2015). PCR is a method that can be used to overcome the problem of multicollinearity on predictor variables, because a multiple regression model needs among predictors uncorrelated or not multicollinear (Wigena and Djuraidah, 2014). In summary, the PCR method has two parts: 1) obtaining flow predictors through a Principal Component Analysis (PCA) applied to the SLP field, and 2) the construction of a multiple regression model that use the selected predictors to simulate de streamflow.

Summarizing, PCA or Empirical Orthogonal Function (EOF) analysis is an orthogonal transformation that reduces an original dataset containing a large number of possibly correlated variables to a dataset usually containing many fewer uncorrelated variables (Sahriman et al., 2014). The space variance of our variable's distribution is given by the eigenvector maps or the before mentioned EOFs. The eigenvalues of EOFs indicate the amount of variance accounted for by a pattern. The projection of the time series observations on to the eigenvectors are called principal components (PCs) (Rodríguez-Puebla et al., 1998). The PCA can be performed in S or T modes (Lorenzo-Lacruz et al., 2011). The S mode identifies regions in which the temporal variation of our variables have the same pattern. The S mode can be therefore used to identify general temporal patterns in the analyzed variable. Using this approach we can obtain an additional non-correlated set of variables called principal components, PCs, that are the linear combinations of the originals. The coefficients of such combinations are called loading factors, and represent the correlations of the principal component with each original variable. A more detailed description about PCA can be seen in the Appendix A. In the following, a mathematical description of the PCR method is presented. As PCs are uncorrelated, they can be used in regression models avoiding multicollineary problems between predictors.

Let $Q_{calib}(t, x)$ and $Q_{valid}(t, x)$ denote the observed winter streamflow from the gauging stations and reservoirs (predictands) at the q grid points $x = 1, \ldots, q$ for

observation time $t = 1, \ldots, m$ for the calibration period 1950–95 and $t = m+1, \ldots, n$ for the validation period 1996–2011. The $SLP_{calib}(t, y)$ and $SLP_{valid}(t, y)$ from the reanalysis data are the predictor data field at p SLP grid points $y = 1, \ldots, p$ at the same periods. The first step in PCR consists of performing a PCA (see Appendix A) (Preisendorfer and Mobley, 1988) of the covariance matrix from predictor input data, that is, the SLP_{calib}. From this PCA the SLP spatio-temporal variability can be analyzed from the empirical orthogonal functions (EOFs, eigenvectors of the covariance matrix) and the principal component series (PCs, projections of the observed SLP anomalies on the EOFs).

A key aspect is the choice of the number k of EOFs to retain, but there are no definitive rules to choose it. For this selection we have taken into account that they explain a high percentage of variance and a significant correlation between the different PCs with streamflow series.

Once the main PCs of SLP_{calib} have been selected, the PCR method has been applied to model the winter streamflow following the scheme proposed by Li and Smith (2009). So, the regression model between the PCs of the SLP_{calib} and Q_{calib} have been fitted, obtaining the regression coefficients (b_i and a_{ij},) by the usual least squares method, that is

$$Q_{calib}(i, t) = b_i + a_{ij} PC_j + error(i) \tag{3.1}$$

where i =1,... q and j =1,... k.

For the validation period (1996–2011), the predictor variables (PCs*) are obtained projecting the SLP_{valid} onto the EOFs of the SLP. Then the Q_{valid} is calculated by applying the regression models:

$$Q_{valid}(i, t) = b_i + a_{ij} PC_j^* \tag{3.2}$$

The following step is to recalibrate the models using the whole observational period (1950–2011) in order to take into account the recent variability of the fields within the regression models. These last models are the statistical downscaled (SD) models.

Finally, we obtain streamflow projections for the period 2071-2099 by applying the obtained downscaling model to the SLP data derived from the GCM simulations under the three chosen RCPs scenarios (RCP2.6, RCP4.5 and RCP8.5). In other to correct the models bias, the Delta method (Hijmans et al., 2005; Palomino-Lemus et al., 2015) was used, so the projected changes are calculated as the difference between the modeled streamflow using historical and RCPs output for each model.

The difference of the mean values for present and future downscaled streamflow was evaluated by the Wilcoxon–Mann–Whitney rank sum test. If the p value is lower than 0.05, the mean values for both periods are significantly different at 95%, while if it is higher than 0.1 they are not different with a significance level of 90%, for example.

Chapter 4

Results

In this section the results of the analysis are shown. First, the spatio-temporal variability of the winter SLP from the reanalysis data is instigated. Secondly, a validation of the SLP outputs of the GCMs has been carried out in order to determine if the models are able to reproduce the main modes of variability of the SLP for present climate. From this point, the correlation between the variability modes of the SLP and the streamflow will be computed in order to determine the potential predictors for the streamflow, which will be used in a regression model. The downscaled model obtained for present climate will be finally used for obtaining the climate change projections of winter streamflow.

4.1 Spatio-temporal variability of SLP

For starting, the stability of the predictor field, winter SLP, is analyzed computing the average SLP fields, their patterns of variability and their associated variances for each database, reanalysis and GCMs. For this end, Figure 4.1 shows a comparison of the averaged SLP field from the reanalysis data and the three models that we will use in this work. On the map from the NCEP data we can see a dipolar pattern with two action centers, one with high SLP values around the latitude band of 30°-40°N, and another one, presenting lower values of SLP located closed to Iceland. The CESM model presents the same structure. However, the IPSL-CM5A-MR has similar shape but with a lower gradient between Azores and Iceland, and also with a SLP overestimation over Greenland. Lastly, MIROC5 presents a structure that approximates to the NCEP data, although it doesn't capture the regions around the centers properly, maybe related with the coarser resolution of this model.

The next step is the Empirical Orthogonal Functions (EOF) analysis, used to identify the main variability patterns of winter SLP. This PCA obtains patterns (EOFs) that facilitate the comparison of the climate variability reproduced by the reanalysis data (NCEP) and the models.

For this analysis, the first six modes of winter SLP variability identified by the PCA of the reanalysis data in the period 1950–2011, which explain 85.7% of the total variance, were retained. The time series of these modes are shown in Figure

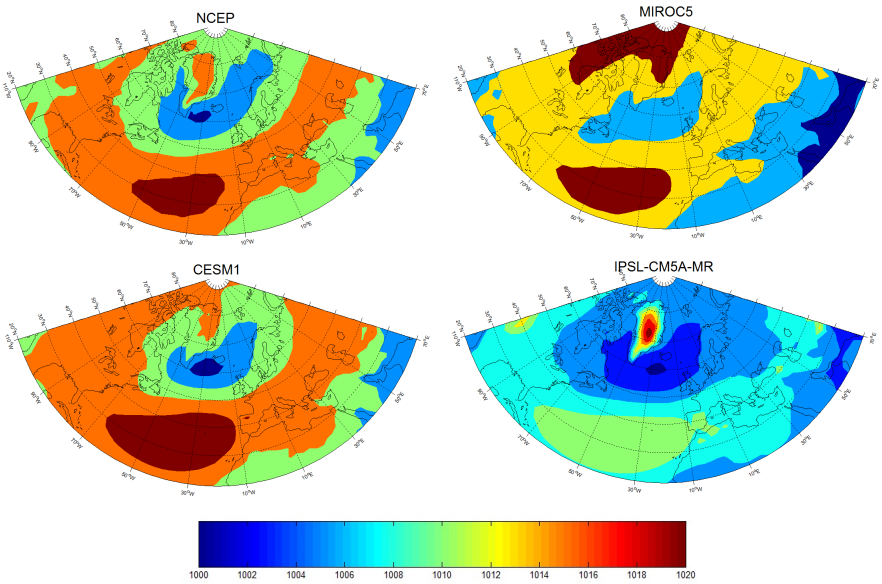

Figure 4.1 – Average patterns of the SLP (mb) of the reanalysis data (1950-2011), MIROC5, CESM1 and IPSL-CM5A-MR data (1951-2005).

4.2, while the associated spatial patterns (EOFs) are shown in Figure 4.3. Similarly, Figures 4.4 to 4.6 show the results of the PCA to the winter SLP outputs of the three GCMs used, for the period historical (1951-2005).

For reanalysis data, EOF1 explains the majority (46.48%) of the variance for the winter SLP field, with one positive correlated center located over Greenland and another negative correlated center over the Mediterranean and the central North Atlantic. This spatial pattern corresponds clearly to the NAO. The second EOF, which explains 11.90% of winter SLP variance, exhibits a positive center located in the North Atlantic. EOF3 (10.86% of variance) represents a tripolar structure with a high negative correlation center in northern Europe. EOF4 (9.93% of variance) also shows a tripolar structure with a pattern with high negative loading factors centered on the British Isles. EOF5 and EOF6 (3.54% and 3.02%, respectively) account for only 14.43% of the SLP variance and show different action centers over the study region with lower correlations.

Figure 4.2 shows the PCs associated with the EOFs. These time series present for all the cases an important interannual variability. Note that for the PC1 decadal variability is also apparent. To explore the physical meaning of these spatial modes, correlations between the PC series and several teleconnection indices for the period 1951-2010 have been computed, and they are shown in the table 4.1 . As expected, the time series of the first EOF is strongly linked with the NAO (r = -0.55), and it exhibits a significant increase in the year 2010. PC1 is also linked to both the EA (r = -0.33) and the EA-WR index (r = -0.27). Also, the third PC series is linked with the SCAND index (r = 0.26).

To check if the model data represent the real current conditions for winter SLP

field, the spatial patterns of the SLP variability (EOFs) from the reanalysis data (1950-2011) have been compared to those obtained from the model outputs also for the present time (1951-2005), and they can be seen in Figures 4.4, 4.5 and 4.6 for the models MIROC5, CESM1 (CAM5) and IPSL-CM5A-MR, respectively.

For the first EOF, all models show similar structures and have almost the same percentage of explained variance than the EOF1 from the reanalysis data, except for the MIROC5 model, whose structure is mainly the same but spread to the west, being its variance a little bit lower. EOF2 is characterized by a positive center located in the North Atlantic for the NCEP data , being a negative center for the CESM1 (CAM5) and IPSL-CM5A-MR models, which explain a bit more of variance. On the other hand, the model MIROC5 represents a structure that is further from the EOF of the reanalysis data, although its variance is higher. For EOF3, all models show similar structures to the EOF3 from reanalysis data, and showing also the same percentage of explained variance. Regards the fourth EOF, it is the CESM1 (CAM5) model which is the nearest to represent the EOF4 from the reanalysis data, being the MIROC5 model which presents a more differentiated pattern to the NCEP data. Again, the variance explained is very similar. Finally, EOF5 and EOF6 represent different structure between them and from the NCEP data, and their variance is almost similar.

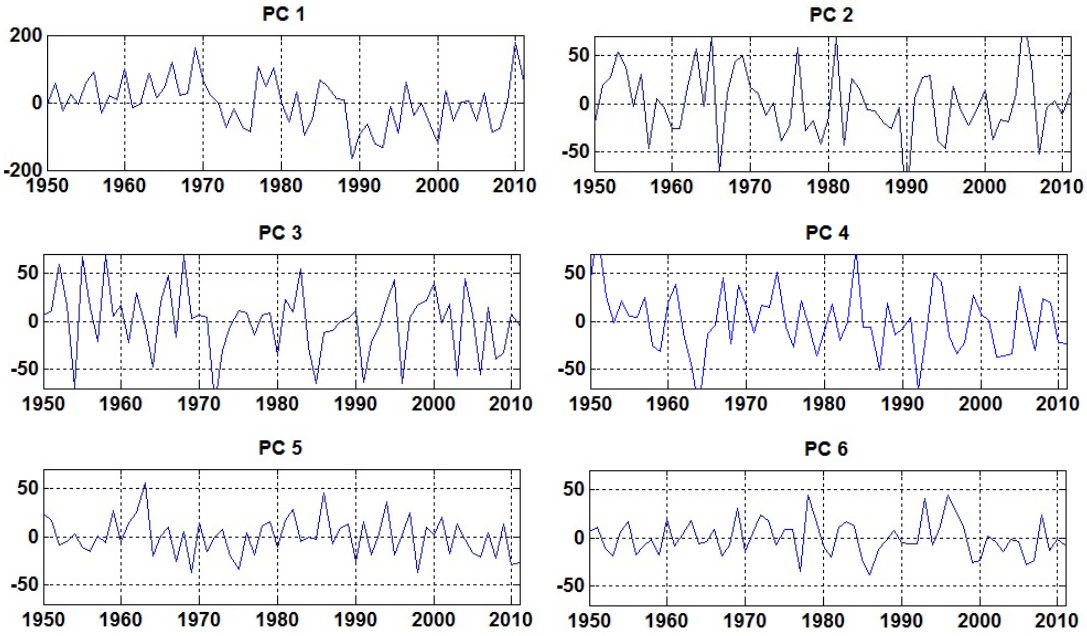

Figure 4.2 – Principal Components of the six leading SLP modes.

In order to select adequate predictors for winter Douro streamflow that can be used in in the regression model, correlations between streamflow time series and the six leading PCs of the SLP from reanalysis data for the period 1950-2010 have been calculated. PCs that show significant correlations at 95% confidence level with the

streamflow time series in the Douro River were selected as predictor variables for the regression model. This result is shown in Table 4.2. Note that the first two variability modes and the fifth and sixth (also the fourth but just for the gauging station number 2082) of the winter SLP are significantly associated with winter Douro streamflow. Thus, only these five modes were considered for the development of the regression models.

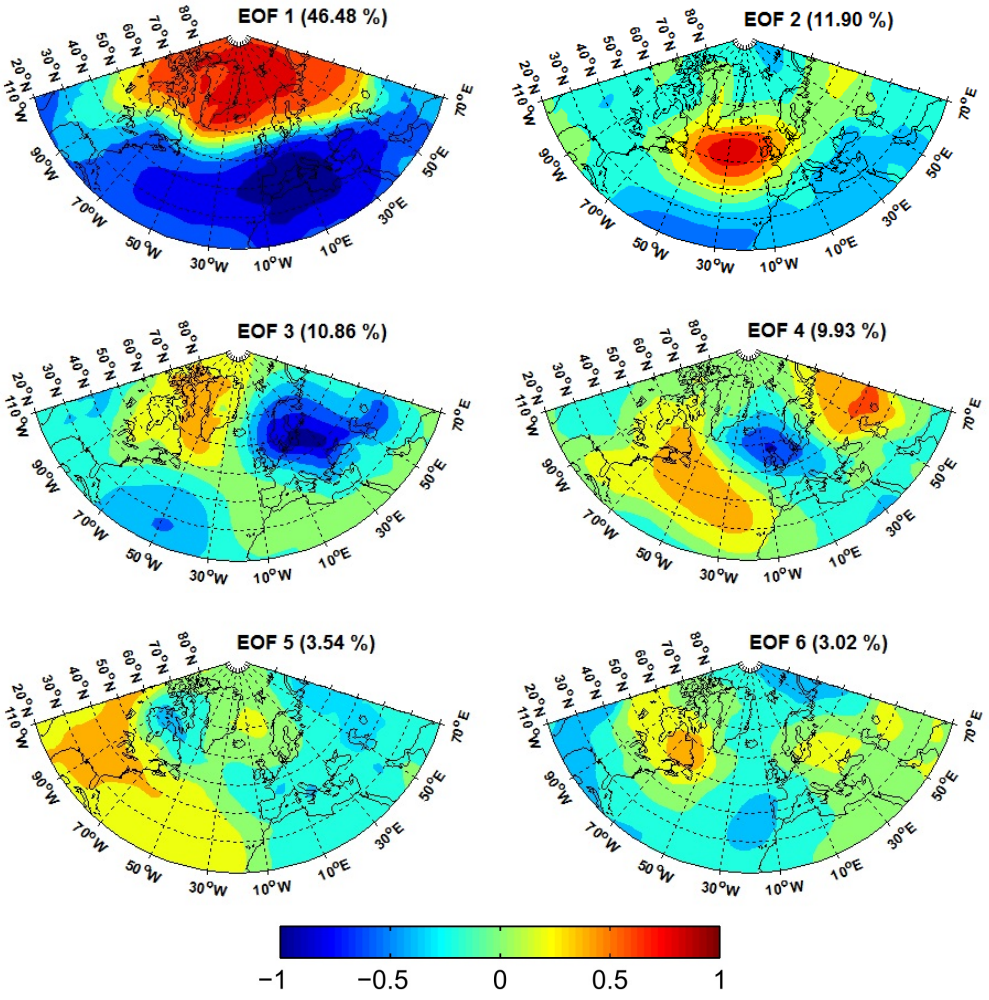

Figure 4.3 – Factor loading of the first six leading Empirical Orthogonal Factors of winter SLP over the study area for the reanalysis data. Variance explained by each mode is indicated in parentheses.

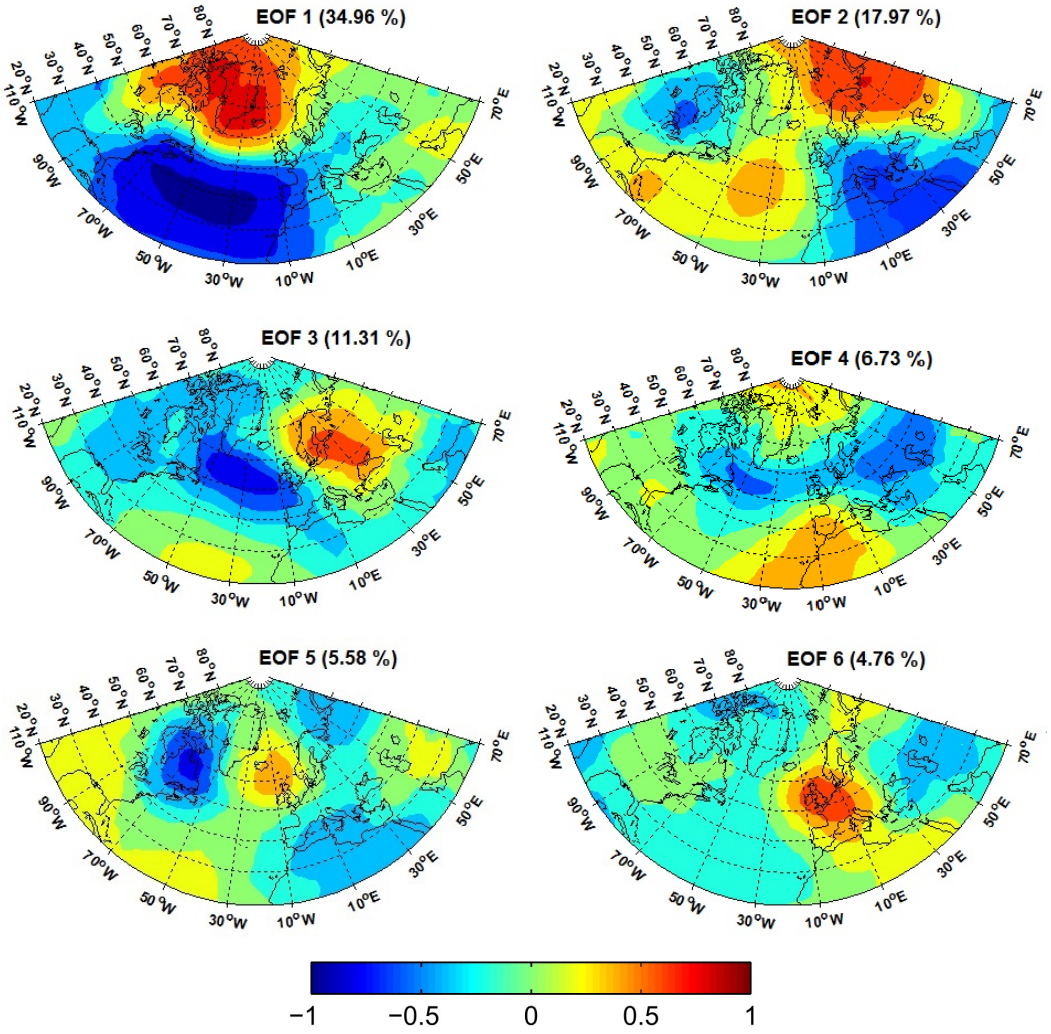

Figure 4.4 – Factor loading of the first six leading Empirical Orthogonal Factors of winter SLP over the study area for the MIROC5 data (1951-2005). Variance explained by each mode is indicated in parentheses.

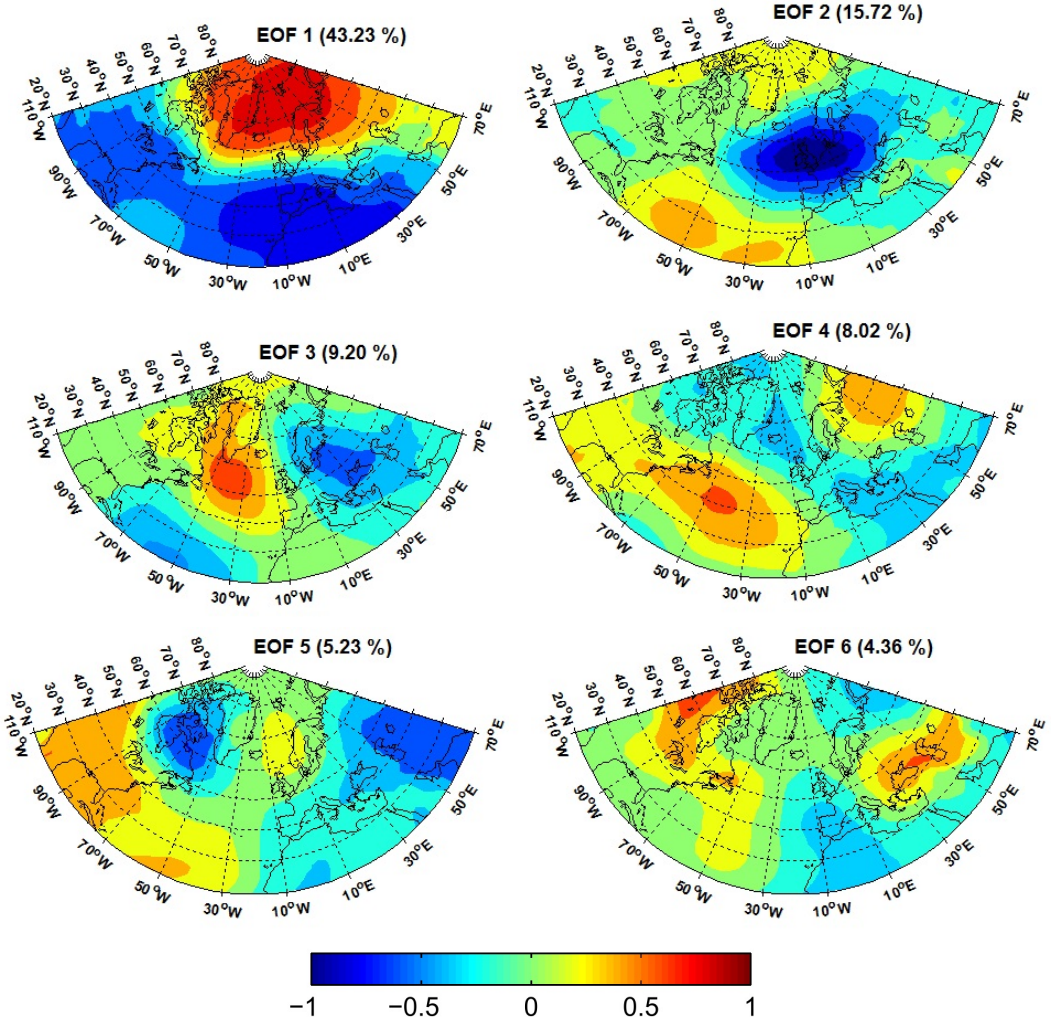

Figure 4.5 – Factor loading of the first six leading Empirical Orthogonal Factors of winter SLP over the study area for the CESM1(CAM5) data (1951-2005). Variance explained by each mode is indicated in parentheses.

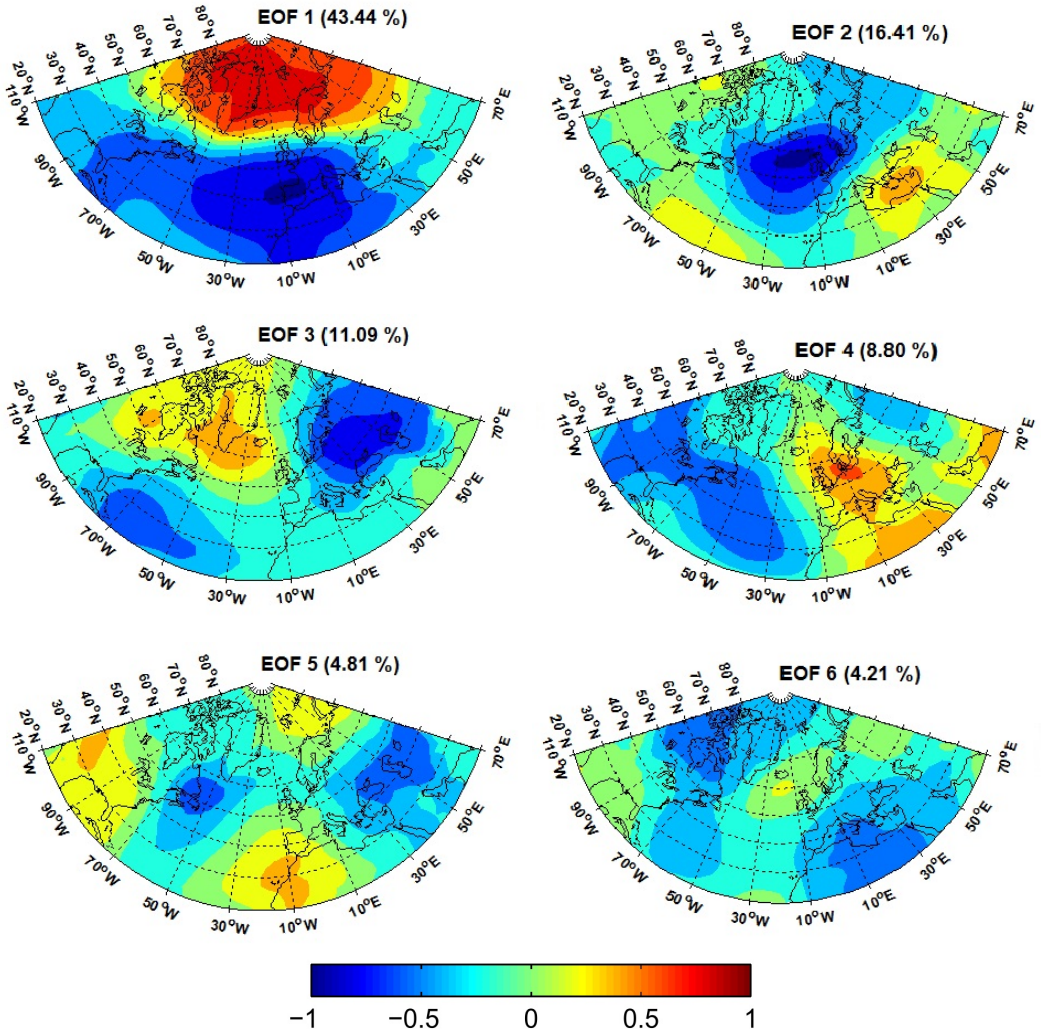

Figure 4.6 – Factor loading of the first six leading Empirical Orthogonal Factors of winter SLP over the study area for the IPSL-CM5A-MR data (1951-2005). Variance explained by each mode is indicated in parentheses.

	PC1	PC2	PC3	PC4	PC5	PC6
NAO	**-0.557**	-0.179	0.131	0.193	-0.001	0.007
EA	**-0.333**	-0.047	-0.150	-0.014	0.006	0.080
SCAND	0.025	0.043	**0.268**	-0.106	0.076	0.001
EA-WR	**-0.279**	-0.043	-0.019	0.182	0.071	0.133

Table 4.1 – Correlations between the six leading PCs of the winter SLP reanalysis data and the teleconnection indices NAO, EA, SCAND and EA-WR, for the period 1951-2010. Significant correlations at 95% confidence level are shown in bold.

	PC1	PC2	PC3	PC4	PC5	PC6
2030	**-0.647**	**-0.248**	-0.067	0.093	**0.255**	0.178
2031	**0.608**	**-0.273**	-0.048	-0.011	**0.259**	0.117
2036	**0.575**	**-0.243**	-0.021	0.024	**0.235**	0.165
2062	**0.608**	**-0.279**	-0.020	-0.044	0.191	**0.225**
2082	**0.635**	**-0.237**	-0.157	**-0.235**	0.142	**0.233**
2002	**0.620**	**-0.288**	0.001	-0.075	0.191	**0.240**
2003	**0.597**	**-0.294**	0.013	-0.065	0.211	**0.242**
2029	**0.633**	**-0,255**	-0.021	-0.102	0.166	**0.263**

Table 4.2 – Correlations between the six leading PCs from winter SLP of reanalysis data and the selected gauging stations (dark gray) and reservoirs (light gray). Significant correlations at the 95% confidence level are shown in bold.

4.2 Principal component regression models for the streamflow

As was described in the Chapter 3, we used the principal component regression (PCR) method to build the forecasting model for the streamflow. For this analysis, we retained the first two variability modes of SLP field in all stations, but also the fourth, fifth and sixth PCs appeared in some cases as significant. As mentioned in the Chapter 3, the training period 1950–1995 was used as calibration period, and the period 1996–2011 to verify the model. The objective was to develop a robust model that provides a downscaled prediction for the streamflow given a predictor large-scale SLP field.

Figure 4.7 compares the predicted and observed winter streamflow for all selected gauging stations and reservoirs. Meanwhile, Table 4.3 presents a summary with the statistics obtained from the regression model, showing the correlations values between the observed and predicted streamflow, significant at the 95% level, and also the root-mean-square error (RMSE), for both periods.

In general the regression model works properly, performing well during the training period, in years like 1960 and 1966, but a bit worse during the subsequent verifi-

cation period, although it clearly fails when estimating peak values as the high flows registered during the years 1979 and 2001, which correspond to very rainy years in the region. We may attribute to these years the principal cause of the high RMSE values obtained.

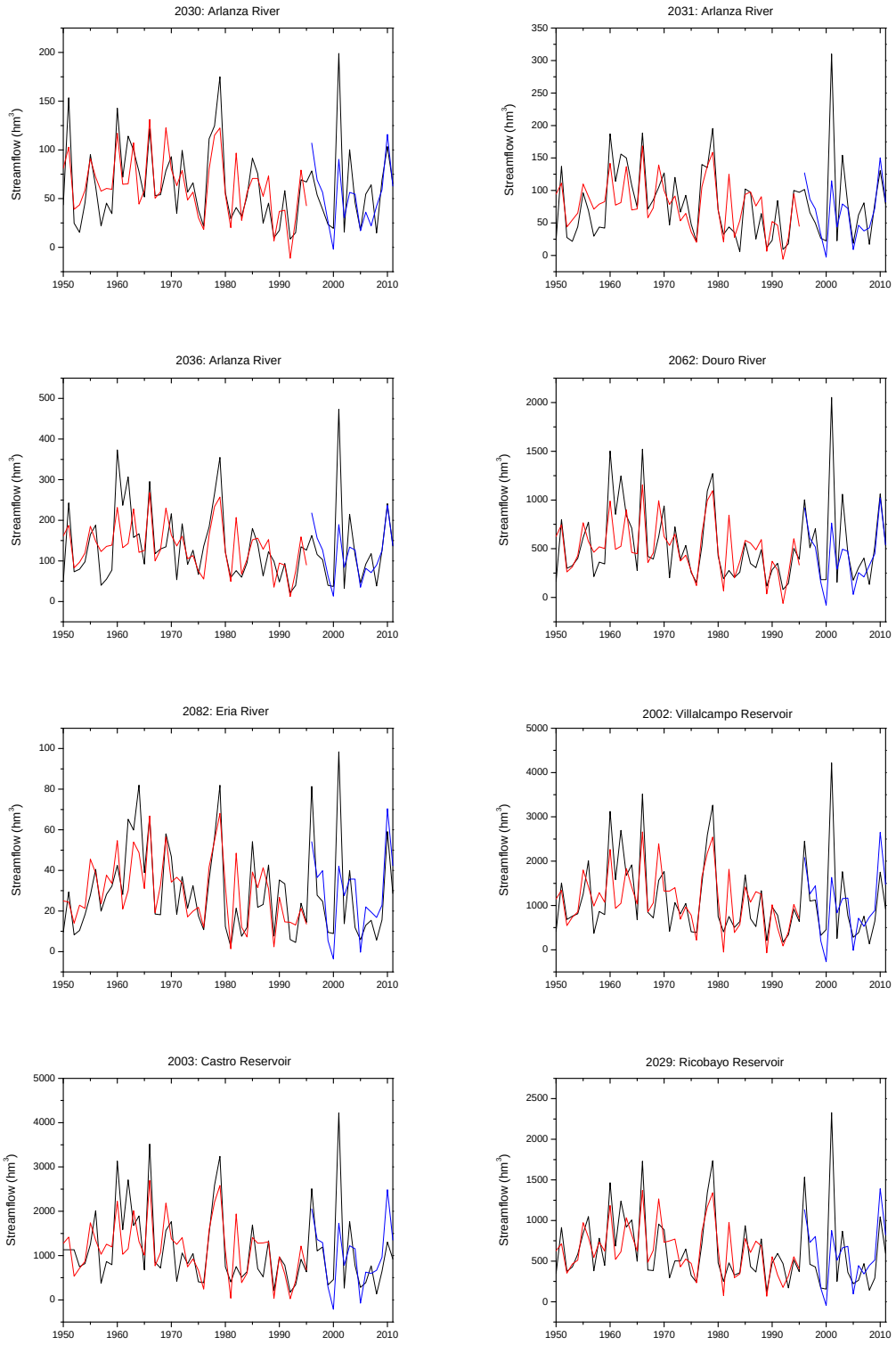

Figure 4.7 – Streamflow series for the gauging stations 2030, 2031, 2036, 2062 and 2082 and the reservoirs 2002, 2003 and 2029. The observed streamflow (1950-2011) is represented by the black line, the prediction during the training period (1950-1995) corresponds to the red line and the prediction for the validation period (1996-2011) is represented by the blue line.

	Training period (1950-1995)		Verification period (1996-2011)	
Station	r	RMSE	r	RMSE
2030	0.79	23.99	0.66	34.47
2031	0.76	32.69	0.65	55.70
2036	0.68	61.20	0.68	79.63
2062	0.75	231.51	0.63	373.03
2082	0.78	12.53	0.70	19.04
2002	0.77	516.19	0.63	795.23
2003	0.77	505.22	0.63	783.56
2029	0.80	227.83	0.64	440.82

Table 4.3 – Correlation (r) and root-mean-square error (RMSE) between the observed and predicted streamflow by the regression model, both for the calibration period (1950-1995) and the validation period (1996-2011).

	Recalibration (1950-2011)	
Station	r	RMSE
2030	0.75	26.59
2031	0.72	8.85
2036	0.68	65.63
2062	0.73	55.45
2082	0.76	14.09
2002	0.75	578.14
2003	0.70	611.09
2029	0.75	287.67

Table 4.4 – Correlation (r) and root-mean-square error (RMSE) between the observed and predicted streamflow by the regression model after the recalibration.

Once the downscaling model has been validated, we have recalibrated it using all data, that is, calibrating it again for the full period. In Figure 4.8 we can see the comparison between the observed winter streamflow and the prediction with the recalibration just commented. The correlation coefficients between the observed and predicted values and their RMSE are presented in Table 4.4. It should be noted that there is an improvement in the prediction in respect to the verification period, although the model is not able to reproduce the extreme streamflow values of the last records.

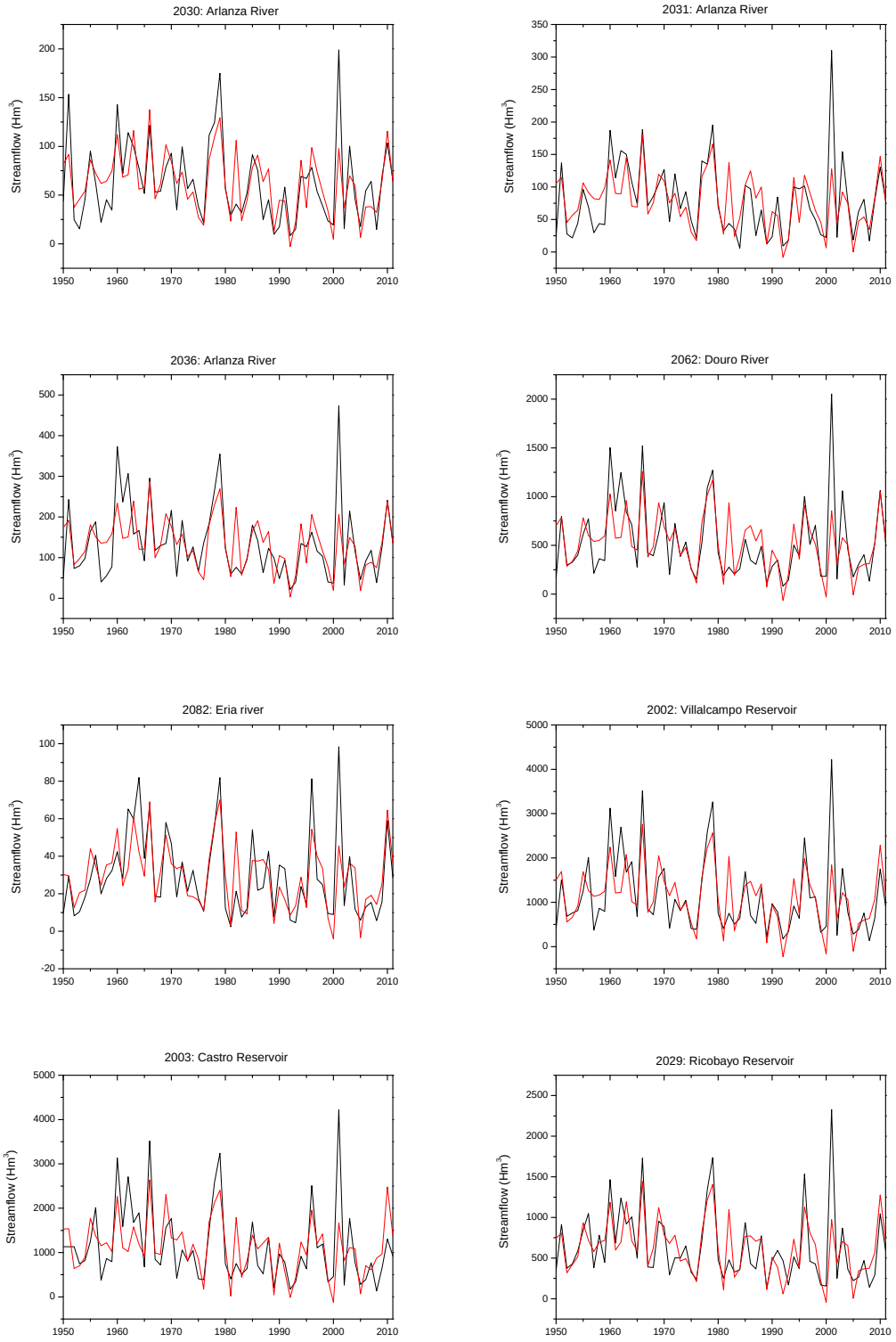

Figure 4.8 – Streamflow series for the gauging stations 2030, 2031, 2036, 2062 and 2082 and the reservoirs 2002, 2003 and 2029. The observed streamflow (1950-2011) is represented by the black line, the prediction after the recalibration for all period (1950-2011) corresponds to the red line.

4.3 Climate change projections

After having established the principal component regression model for the statistic downscaling of the streamflow, and in order to identify the potential impact of the climate change, we have applied it to the SLP data derived from the GCM simulations for both the present (1951-2005) and future (2071-2099) climate under the RCP2.6, RCP4.5 and RCP8.5 scenarios. The results obtained are shown in Tables 4.5, 4.6 and 4.7 for each of the three GCMs, respectively.

In general, for present climate we could say that CESM1 and IPSL-CM5A-MR models present a clear streamflow underestimation, whereas MIROC5 shows important overestimations. Furthermore, there are marked differences between the performance of the different models, being the IPSL-CM5A-MR which better represents the present conditions for most of the stations. Therefore, there are a considerable bias between the observational streamflow data and the present climate estimations from the models, which could be attributed to the tendency of the GCMs to show a more zonal pattern of the SLP than the NCEP data. This bias is taken into account when calculating the winter streamflow projections for the period 2071-2099. Thus, the streamflow differences have been obtained by subtracting the average model values in the present time to the projected future data, being the percentages relative to the modeled average.

As can be seen, the results of the projected changes for later this century show generalized decreases of the winter streamflow for all models and scenarios. As expected, the RCP2.6 scenario presents the lowest decreases, in contrast to RCP8.5, which shows the highest decreases in the winter streamflow for CESM1 and IPSL-CM5A-MR models, but being the RCP4.5 scenario which surprisingly projects the greatest changes for MIROC5. The stations 2002, 2003 and 2029 suffer the biggest changes, due to the fact that are reservoirs and contain the biggest amount of water.

We can see that the p value obtained from the Wilcoxon–Mann–Whitney rank sum test is higher for the results obtained with the CESM1 and IPSL-CM5A-MR models, being the lowest values for the RCP8.5 scenario, so for this scenario the projected streamflow changes are significant for some locations. On the other hand, the MIROC5 model presents low p values in general, therefore, it shows the most significant changes, above all for the RCP4.5 in all stations, which ranges from -12.42% to -67.52%. It should be remarked the projected decrease by CESM1 in the stations 2031 and 2029 for the RCP8.5 scenario, reaching decreases of around -40%. It is also very significant the projected decrease by the IPSL-CM5A-MR model for the RCP4.5 and RCP8.5 scenarios in the station 2029, with -63.57% and -91.90%, respectively.

These declines are consistent with the results obtained by Esteban Parra et al. (2014) for another peninsular river. Moreover, the results also agree with the decrease in projected precipitation obtained using WRF simulation with CCSM3 model as boundary conditions (Argüeso et al., 2012). This model is the predecessor of the CESM1 used in this work.

On the other hand, the Douro River streamflow is not only influenced by precip-

itation. Temperature is another factor affecting the streamflow, regulating evapotranspiration processes in the basin as well as snow, which contributes to the spring flow (López-Moreno and García-Ruiz, 2004). While precipitation during the winter in large part of the IP, particularly in the Douro Valley, is controlled largely by atmospheric circulation, mainly through the impact of the NAO (Esteban-Parra et al., 1998)), this pattern slightly affects the behaviour of the winter temperatures form (Esteban-Parra et al., 2003).

Several studies (e.g. IPCC, 2013) show that for various scenarios, including RCP8.5, the average increases in temperature in winter in the 2071-2099 period obtained using ECHAM5 as WRF input are around 2.5 °C compared to the period 1970-2000. However, this study does not allow to clarify the direct impact of temperature on the streamflow in the sense of knowing whether the obtained streamflow increase in the present climate may reflect, for example, the contribution of snowmelt during the winter instead of in spring.

	Present (1951-2005)				Future (2071-2099)		
Station	Source	Amount (hm^3)	Diff with obs (hm^3)	Diff(%)	Amount (hm^3)	Diff with (1950-2011) (hm^3)	Diff(%)
2030	Obs	62.66					
	GCM	97.93	35.27	56.28			
	RCP2.6				89.59 (0.030)	-8.34	-8.51
	RCP4.5				62.15 (10^{-7})	-35.78	-36.53
	RCP8.5				84.13 (0.006)	-13.80	-14.09
2031	Obs	78.87					
	GCM	110.37	31.50	39.93			
	RCP2.6				102.74 (0.120)	-7.63	-6.91
	RCP4.5				96.65 (0.039)	-13.71	-12.42
	RCP8.5				104.09 (0.332)	-6.27	-5.68
2036	Obs	134.46					
	GCM	206.41	71.95	53.51			
	RCP2.6				203.04 (0.604)	-3.36	-1.62
	RCP4.5				122.12 (10^{-10})	-84.29	-40.83
	RCP8.5				200.63 (0.572)	-5.78	-2.80
2062	Obs	534.66					
	GCM	811.20	276.54	51.72			
	RCP2.6				724.85 (0.058)	-86.35	-10.64
	RCP4.5				446.01 (10^{-6})	-365.18	-45.01
	RCP8.5				745.12 (0.235)	-66.08	-8.14
2082	Obs	29.71					
	GCM	44.90	15.19	51.12			
	RCP2.6				41.83 (0.275)	-3.07	-6.83
	RCP4.5				21.34 (10^{-6})	-23.56	-52.47
	RCP8.5				42.92 (0.486)	-1.98	-4.40
2002	Obs	1123.91					
	GCM	1750.10	626.19	55.71			
	RCP2.6				1551.11 (0.059)	-198.99	-11.37
	RCP4.5				906.40 (10^{-6})	-843.70	-48.20
	RCP8.5				1598.43 (0.243)	-151.67	-8.66
2003	Obs	1132.25					
	GCM	1719.14	586.89	51.83			
	RCP2.6				1521.72 (0.055)	-197.41	-11.48
	RCP4.5				927.84 (10^{-6})	-791.29	-46.02
	RCP8.5				1570.45 (0.243)	-148.68	-8.64
2029	Obs	634.29					
	GCM	980.42	346.13	54.56			
	RCP2.6				1307.76 (10^{-6})	327.34	33.38
	RCP4.5				318.43 (10^{-9})	-661.99	-67.52
	RCP8.5				1244.11 (10^{-4})	263.68	26.89

Table 4.5 – Average streamflow values obtained by the MIROC5 model for both the present (1950-2011) and future (2071-2099). A comparison between observed and downscaled GCM value for both periods. In column 6 the p value results from Wilcoxon–Mann–Whitney rank sum test are shown in parentheses.

	Present (1951-2005)				Future (2071-2099)		
Station	Source	Amount (hm^3)	Diff with obs (hm^3)	Diff(%)	Amount (hm^3)	Diff with (1950-2011) (hm^3)	Diff(%)
2030	Obs	62.66					
	GCM	46.46	-16.20	-25.85			
	RCP2.6				47.70 (0.977)	1.24	2.66
	RCP4.5				38.41 (0.184)	-8.05	-17.32
	RCP8.5				30.04 (0.008)	-16.42	-35.34
2031	Obs	78.87					
	GCM	61.53	-17.34	-21.98			
	RCP2.6				58.41 (0.604)	-3.12	-5.07
	RCP4.5				50.17 (0.175)	-11.36	-18.46
	RCP8.5				36.64 (0.002)	-24.89	-40.45
2036	Obs	134.46					
	GCM	96.17	-38.29	-28.47			
	RCP2.6				96.16 (0.925)	-0.01	-0.01
	RCP4.5				91.71 (0.638)	-4.45	-4.62
	RCP8.5				68.43 (0.016)	-27.74	-28.84
2062	Obs	534.66					
	GCM	392.50	-142.16	-26.58			
	RCP2.6				371.89 (0.631)	-20.61	-5.25
	RCP4.5				304.83 (0.109)	-87.67	-22.33
	RCP8.5				257.17 (0.013)	-135.33	-34.47
2082	Obs	29.71					
	GCM	12.74	-16.97	-57.11			
	RCP2.6				11.70 (0.457)	-1.04	-8.16
	RCP4.5				8.33 (0.129)	-4.41	-34.61
	RCP8.5				9.10 (0.166)	-3.64	-28.57
2002	Obs	1123.91					
	GCM	802.79	-321.12	-28.57			
	RCP2.6				755.94 (0.598)	-46.85	-5.83
	RCP4.5				602.92 (0.097)	-199.87	-24.89
	RCP8.5				500.78 (0.014)	-302.01	-37.62
2003	Obs	1132.25					
	GCM	831.97	-300.28	-26.52			
	RCP2.6				784.72 (0.604)	-47.25	-5.67
	RCP4.5				633.45 (0.103)	-198.52	-23.86
	RCP8.5				542.56 (0.015)	-289.41	-34.78
2029	Obs	634.29					
	GCM	457.79	-176.50	-27.82			
	RCP2.6				368.19 (0.207)	-89.60	-19.57
	RCP4.5				428.74 (0.446)	-29.05	-6.34
	RCP8.5				245.80 (0.002)	-211.99	-46.30

Table 4.6 – As Table 4.5, for the model CESM1.

	Present (1951-2005)				Future (2071-2099)		
Station	Source	Amount (hm^3)	Diff with obs (hm^3)	Diff(%)	Amount (hm^3)	Diff with (1950-2011) (hm^3)	Diff(%)
2030	Obs	62.66					
	GCM	65.97	3.31	5.28			
	RCP2.6				62.15 (0.534)	-3.82	-5.79
	RCP4.5				61.35 (0.604)	-4.61	-6.98
	RCP8.5				63.10 (0.749)	-2.86	-4.33
2031	Obs	78.87					
	GCM	98.82	18.95	25.29			
	RCP2.6				96.65 (0.770)	-2.16	-2.18
	RCP4.5				93.31 (0.631)	-5.50	-5.56
	RCP8.5				84.19 (0.144)	-14.63	-14.80
2036	Obs	134.46					
	GCM	126.05	-8.41	-6.25			
	RCP2.6				122.12 (0.678)	-3.92	-3.10
	RCP4.5				112.45 (0.337)	-13.59	-10.78
	RCP8.5				93.21 (0.015)	-32.83	-26.04
2062	Obs	534.66					
	GCM	465.60	-69.06	-12.91			
	RCP2.6				446.01 (0.785)	-19.58	-4.20
	RCP4.5				485.13 (0.770)	19.53	4.19
	RCP8.5				396.18 (0.474)	-69.42	-14.90
2082	Obs	29.71					
	GCM	20.19	-9.52	-32.04			
	RCP2.6				21.34 (0.821)	1.15	5.69
	RCP4.5				21.65 (0.685)	1.46	7.23
	RCP8.5				18.17 (0.572)	-2.01	-9.95
2002	Obs	1123.91					
	GCM	950.92	-172.99	-15.39			
	RCP2.6				906.40 (0.792)	-44.52	-4.68
	RCP4.5				1001.63(0.727)	50.71	5.33
	RCP8.5				799.20 (0.492)	-151.72	-15.95
2003	Obs	1132.25					
	GCM	970.25	-162.00	-14.30			
	RCP2.6				927.84 (0.799)	-42.40	-4.37
	RCP4.5				1027.33 (0.685)	57.07	5.88
	RCP8.5				835.50 (0.547)	-137.74	-14.19
2029	Obs	634.29					
	GCM	497.82	-136.47	-21.51			
	RCP2.6				318.43 (0.048)	-179.39	-36.03
	RCP4.5				181.33 (0.001)	-316.49	-63.57
	RCP8.5				40.29 (0.00004)	-457.53	-91.90

Table 4.7 – As Table 4.5, for the model IPSL-CM5A-MR.

Chapter 5

Conclusions

In this study we have obtained climate change projections for winter Douro River streamflow under the scenarios RCP2.6, RCP4.5 and RCP8.5, for the period 2071-2099 using the outputs of three GCMs (MIROC5, CESM1 and IPSL-CM5A-MR). The methodology that we have followed has been the PCR. The PCA applied to the winter SLP reanalysis data from the NCEP showed the existence of six leading variability modes, which explain 85.7% of the total variance. Hence, we analyzed the association between these resulting principal components and the streamflow series from the eight selected gauging stations and reservoirs in order to use the SLP PC series as predictor variables in a multiple regression model.

The statistic models built for the eight stations showed in general a good representation both for the calibration and validation periods, although they clearly failed at estimating peak values which correspond to very rainy years. After this step, we recalibrated it again for the full period.

Finally, we applied the model data to our regression model, obtaining the streamflow projections, evaluating the difference of the mean values for present and future by the Wilcoxon–Mann–Whitney rank sum test.

Our general conclusions are the following:

- The North Atlantic Oscillation is the teleconnection pattern that mainly controls the winter precipitation variability in the west part of the Iberian Peninsula, and therefore it is directly reflected in the winter seasonal flow of the Douro River. This pattern is mainly represented by the first SLP EOF.

- For the downscaling model, there is an improvement in the regression model during the verification period after having recalibrated it for the full period. However, the model fails at estimating peak values related to very rainy years.

- CESM1 and IPSL-CM5A-MR models present a clear underestimation of the present streamflow, whereas MIROC5 shows important overestimations. Thus, that bias has effects on the results of the future projections.

- The Global Circulation Models MIROC5, CESM1 and IPSL-CM5A-MR clearly show generalized decreases of the Douro River winter streamflow for the period

2071-2099, under the scenarios RCP2.6, RCP4.5 and RCP8.5, being particularly significant for MIROC5 model and the RCP4.5 scenario, in which it projects decreases from -12.42% to -67.52%.

It should be noted that the downscaling method in this work can only represent the changes in the streamflow, which are principally derived from the changes in the rain, linked to changes in the atmospheric circulation as we only used one predictor field (SLP) in the downscaling model. For this reason, this study may lead to subsequent research in order to demonstrate that the changes in the streamflow are also linked to other predictor fields, e.g. the temperature, or perform climate change projections for another river basin of the Iberian Peninsula.

List of Figures

List of Tables

List of Acronyms

AIM Asia-Pacific Integrated Model

AOGCM Atmosphere–Ocean General Circulation Model

AR4 Fourth Assessment Report

AR5 Fifth Assessment Report

CAM Community Atmosphere Model

CCSM3 Community Climate System Model Version 3

CCSR Center for Climate System Research

CEDEX Centro de Estudios y Experimentación de Obras Públicas

CESM Community Earth System Model

EA East Atlantic

EA/WR Eastern Asia/Western Russia

EOF Empirical Orthogonal Function

GCAM Global Change Assessment Model

GCM Global circulation model

GHG Greenhouse Gases

IIASA International Institute for Applied Systems Analysis

IP Iberian Peninsula

IMAGE Integrated Model to Assess the Global Environment

IPCC Intergovernmental Panel on Climate Change

IPSL Institut Pierre Simon Laplace

MESSAGE Model for Energy Supply Systems And their General Environmental impact

MIMAM Ministerio de Medio Ambiente

MIROC Model for Interdisciplinary Research on Climate

NCAR National Center for Atmospheric Research

NCEP National Centers for Environmental Prediction

NIES National Institute for Environmental Studies

NAO North Atlantic Oscillation

PCA Principal Component Analysis

PC Principal component

PCR Principal Component Regression

RCM Regional climate model

RCP Representative Concentration Pathways

RF Radiative forcing

RMSE Root-mean-square error

SCAND Scandinavia

SD Statistical downscaled

SLP Sea Level Pressure

SRES Special Report on Emission Scenarios

TAR Third Assessment Report

TCP Teleconnection pattern

WMGHG Well-mixed greenhouse gas

WMO World Meteorological Organization

WRF Weather Research and Forecasting Model

Appendix A

Principal Component Analysis

The PCA is a multivariate technique that transforms the original set of interrelated data to a new coordinate system such that the new variables are uncorrelated and are ordered so that the first few retain most of the variation present in the original dataset (Jolliffe, 2002).

Therefore, only keeping the few first new variables, most of the variation is still retained and a considerable reduction of the dimensionality of the data is achieved. As a consequence, the interpretation of the dependencies between variables is much more straightforward. Another advantage which is significant within the regionalization framework is that it helps to stabilize measurements for additional statistical analysis such as cluster analysis (Timm, 2002) by reduction of information redundancy.

Suppose a dataset containing K variables that have been measured M times. Let us define a M by K matrix X where according to the standard nomenclature for PCA, the rows represent measurements (or observations) and the columns the different variables. In the particular case of S-Mode PCA, the rows might be the times (days) and the columns the different locations (stations).

Let us also define the matrix of anomalies formed by the K column vectors $X'_k = X_k - \bar{X}_k$, where $\bar{X}_k$ are the means calculated over the M elements of column k.

The new variables or *principal components* are then defined as linear combinations of the $K\mathbf{x'}_k$ that have certain properties:

$$u_m = \sum_{k=1}^{K} (e_{k,1} \cdot \mathbf{x'}_k), \quad m = 1...M \tag{A.1}$$

The new base is composed by the $\mathbf{e}_m$ eigenvectors and the first one $\mathbf{e}_1$ is aligned in the direction in which the data vectors jointly exhibit the most variability. This is the primary property of the principal components: the first linear combination is calculated so that it has the maximum variance, the second one is calculated so that it is orthogonal to the previous principal component and explain as much variance as possible, and so on.

Therefore, the largest eigenvalue λ_1 corresponds to the first eigenvector $\mathbf{e}_1$. The

second-largest eigenvalue λ_2 corresponds to the second eigenvector $\mathbf{e}_2$, which is forced to be orthogonal to $\mathbf{e}_1$ and points to the direction in which $\mathbf{x'}_k$ show the next largest variations. Subsequent eigenvectors are defined similarly, associated with eigenvalues of decreasing magnitude and orthogonal to the previous eigenvectors. The matrix of the transformation can thus be written:

$$U = [E]^T X' \tag{A.2}$$

Owing to the fact that principal components are orthogonal and thus uncorrelated, the covariance matrix of U is diagonal. Taking into account this property, the covariance matrix for the principal components can be obtained by diagonalization of the covariance matrix for the original dataset:

$$[S_x] = X' X'^T$$

$$[S_u] = [E^T][S_x][E] = [E^{-1}][S_x][E] = [\Lambda] \tag{A.3}$$

Which is equal to solve the equation:

$$det([S_x] - \lambda[I]) = 0 \tag{A.4}$$

that allows us to determine the eigenvectors and then calculate the principal components. In addition, the eigenvalues indicate the variance explained by each of the principal components. The fraction of total variation in the original $\mathbf{x}_k$ vectors explained by a certain principal component is proportional to its eigenvalue:

$$Percentage\ of\ variance = \frac{\lambda_m}{\sum_{k=1}^{K}(\lambda_k)} \times 100\% \tag{A.5}$$

The transformation can be reverted and thus the original anomaly vectors can be retrieved from the principal components:

$$X' = [E]U \tag{A.6}$$

Truncation of the principal components

Considering that the objective of PCA is to reduce the information contained in the original data, the number of principal components can be truncated and keep only a fraction of the total variance. There are as many principal components as elements in the vector $\mathbf{x'}_m$. However, atmospheric data usually contains redundant information that is removed by approximating the original vectors by linear combinations of $K*$ eigenvectors, where $K^* < K$:

$$\mathbf{x'}_m \approx \sum_{k=1}^{K^*}(e_{m,k} \cdot \mathbf{u}_k), \quad m = 1...M \tag{A.7}$$

The fraction of the total variance explained by the new reduced base of eigenvectors is thus computed as:

$$Variance\ explained\ (\%) = \frac{\sum_{k=1}^{K^*}(\lambda_k)}{\sum_{k=1}^{K}(\lambda_k)} \tag{A.8}$$

In the atmospheric data, selecting $K^* << K$ usually leads to large variance explained and thus the original large dataset can be reduced to a base composed of very few eigenvectors which explain a substantial proportion of the total variance and thus are easier to interpret. The number of principal components to be retained are still a matter of controversy and different method have been proposed.

Bibliography

Argüeso, D., Hidalgo-Muñoz, J., Gámiz-Fortis, S., Esteban-Parra, M., and Castro-Díez, Y. (2012). High-resolution projections of mean and extreme precipitation over spain using the wrf model (2070–2099 versus 1970–1999). *Journal of Geophysical Research: Atmospheres (1984–2012)*, 117(D12).

Argüeso Barriga, D. (2011). *High-resolution projections of climate change over the Iberian Peninsula using a mesoscale model*. PhD thesis, University of Granada.

Castro, A., Vidal, M. I., Calvo, A. I., Fernandez-Raga, M., and Fraile, R. (2011). May the NAO index be used to forecast rain in Spain? *Atmósfera*, 24(3):251–265.

Chang, B., Guan, J., and Aral, M. M. (2015). Scientific Discourse: Climate Change and Sea-Level Rise. *Journal of Hydrologic Engineering*, 20(1, SI).

Clarke, L., Edmonds, J., Jacoby, H., Pitcher, H., Reilly, J., and Richels, R. (2007). Scenarios of greenhouse gas emissions and atmospheric concentrations. *US Department of Energy Publications*, page 6.

Dasari, H. P., Pozo, I., Ferri-Yáñez, F., Araújo, M. B., et al. (2014). A regional climate study of heat waves over the iberian peninsula. *Atmospheric and Climate Sciences*, 4(05):841.

Duarte, R., Pinilla, V., and Serrano, A. (2014). The water footprint of the Spanish agricultural sector: 1860-2010. *Ecological Economics*, 108:200–207.

Esteban-Parra, M., Pozo-Vázquez, D., Castro-Diez, Y., and Trigo, R. (2003). Nao influence on maximum and minimum temperature of the iberian peninsula. In *14th Symposium on Global Change and Climate Variations, American Meteorological Society, Long Beach, CA, USA, February*.

Esteban Parra, M. J., Hidalgo Muñoz, J., Palomino Lemus, R., Cordoba Machado, S., Gámiz Fortis, S., and Castro Díez, Y. (2014). Proyecciones de cambio climático para el caudal de invierno del río Guadalquivir. in "Cambio climático y cambio global".(Eds Fernández-Montes, S., Rodrigo, F.S.) Serie A, 9, 23-34".

Esteban-Parra, M. J., Rodrigo, F., and Castro-Diez, Y. (1998). Spatial and temporal patterns of precipitation in Spain for the period 1880-1992. *International Journal of Climatology*, 18(14):1557–1574.

Evans, J. and McGregor, J. (2012). Future regional climates. in "The Future of the World's Climate".(Eds A Henderson-Sellers, K Mcguffie) pp. 223–252.

Falkenmark, M., Lindh, G., Lindh, G., and Lindh, G. (1976). *Water for a starving world*. Westview Press Boulder, CO, USA.

Fernandez-Gonzalez, S., del Rio, S., Castro, A., Penas, A., Fernandez-Raga, M., Calvo, A. I., and Fraile, R. (2012). Connection between NAO, weather types and precipitation in Leon, Spain (1948-2008). *International Journal of Climatology*, 32(14):2181–2196.

Fujino, J., Nair, R., Kainuma, M., Masui, T., and Matsuoka, Y. (2006). Multi-gas mitigation analysis on stabilization scenarios using aim global model. *The Energy Journal*, pages 343–353.

Garrote de Marcos, L., Carrasco, M., Javier, F., Pedrosa, L., et al. (2008). Respuestas de adecuación ante los escenarios de cambio climático.

Gómez Navarro, J. J. (2011). *Regional modelling of climate evolution in the last millennium and future projections.* PhD thesis, University of Murcia.

Gómez-Navarro, J. J., Montavez, J. P., Jimenez-Guerrero, P., Jerez, S., Garcia-Valero, J. A., and Gonzalez-Rouco, J. F. (2010). Warming patterns in regional climate change projections over the Iberian Peninsula. *Meteorologische Zeitschrift*, 19(3, 1, SI):275–285. 2nd Lund Regional-Scale Climate Modelling Workshop, Lund, Sweden, May 04-08, 2009.

González-Zeas, D., Garrote, L., and Iglesias, A. (2010). Análisis hidrológico de los escenarios de cambio climático en espana. *Unpublished DEA from Ph. D. Thesis, Technical Universtiy of Madrid, Spain.*

Hijioka, Y., Matsuoka, Y., Nishimoto, H., Masui, T., and Kainuma, M. (2008). Global ghg emission scenarios under ghg concentration stabilization targets. *Journal of Global Environment Engineering*, 13:97–108.

Hijmans, R. J., Cameron, S. E., Parra, J. L., Jones, P. G., Jarvis, A., et al. (2005). Very high resolution interpolated climate surfaces for global land areas. *International journal of climatology*, 25(15):1965–1978.

Hurrell, J. W. (1995). Decadal trends in the north atlantic oscillation: regional temperatures and precipitation. *Science*, 269(5224):676–679.

IPCC (2001). *Climate Change 2001: The Scientific Basis. Contribution of Working Group I to the Third Assessment Report of the Intergovernmental Panel on Climate Change [Houghton, J.T., Y. Ding, D.J. Griggs, M. Noguer, P.J. van der Linden, X. Dai, K. Maskell, and C.A. Johnson (eds.)].*

IPCC (2007). *Climate Change 2007: The Physical Science Basis. Contribution of Working Group I to the Fourth Assessment Report of the Intergovernmental Panel on Climate Change*. Cambridge University Press, New York, 2007.

IPCC (2013). *Climate Change 2013: The Physical Science Basis. Contribution of Working Group I to the Fifth Assessment Report of the Intergovernmental Panel on Climate Change [Stocker, T.F., Qin, D., Plattner, G.-K., Tignor, M., Allen, S.K., Boschung, J., Nauels, A., Xia, Y., Bex V., Midgley, P.M. (eds.)]*. Cambridge University Press, Cambridge, United Kingdom and New York, NY, USA, 1535 pp.

Jenkinson, A. and Collison, F. (1977). An initial climatology of gales over the north sea. *Synoptic climatology branch memorandum*, 62:18.

Jolliffe, I. (2002). *Principal Component Analysis*. Springer-Verlag, 2nd edition.

Kawale, J., Liess, S., Kumar, A., Steinbach, M., Ganguly, A. R., Samatova, N. F., Semazzi, F. H., Snyder, P. K., and Kumar, V. (2011). Data guided discovery of dynamic climate dipoles. In *CIDU*, pages 30–44.

Li, Y. and Smith, I. (2009). A statistical downscaling model for southern australia winter rainfall. *Journal of climate*, 22(5):1142–1158.

López-Moreno, J. and García-Ruiz, J. M. (2004). Influence of snow accumulation and snowmelt on streamflow in the central spanish pyrenees. *Hydrological Sciences Journal*, 49(5).

Lorenzo-Lacruz, J., Vicente Serrano, S. M., López-Moreno, J. I., González-Hidalgo, J. C., Morán-Tejeda, E., et al. (2011). The response of Iberian rivers to the North Atlantic Oscillation. *Hydrology and Earth System Sciences*, 15(8):2581–2597.

Meinshausen, M., Raper, S. C. B., and Wigley, T. M. L. (2011a). Emulating coupled atmosphere-ocean and carbon cycle models with a simpler model, MAGICC6-Part 1: Model description and calibration. *Atmospheric Chemistry and Physics*, 11(4):1417–1456.

Meinshausen, M., Smith, S. J., Calvin, K., Daniel, J. S., Kainuma, M. L. T., Lamarque, J.-F., Matsumoto, K., Montzka, S. A., Raper, S. C. B., Riahi, K., Thomson, A., Velders, G. J. M., and van Vuuren, D. P. P. (2011b). The RCP greenhouse gas concentrations and their extensions from 1765 to 2300. *Climatic Change*, 109(1-2, SI):213–241.

MIMAM (1998). *El Libro Blanco del Agua en España*. Ministerio de Medio Ambiente. Diciembre. Madrid, España.

Moreno, J. M., De la Rosa, D., Zazo, C., et al. (2005). Evaluación preliminar de los impactos en España por efecto del cambio climático.

Moss, R. H., Babiker, M., Brinkman, S., Calvo, E., Carter, T., Edmonds, J. A., Elgizouli, I., Emori, S., Lin, E., Hibbard, K., et al. (2008). Towards new scenarios for analysis of emissions, climate change, impacts, and response strategies. Technical report, Pacific Northwest National Laboratory (PNNL), Richland, WA (US).

Nakicenovic, N., Alcamo, J., Davis, G., Vries, B., Fenhann, J., Gaffin, S., Gregory, K., Grübler, A., Jung, T., Kram, T., et al. (2000). Ipcc special report on emissions scenarios, 599 pp. *Univ. Press Cambridge, Cambridge, UK*.

Palomino-Lemus, R., Córdoba-Machado, S., Gámiz-Fortis, S. R., Castro-Díez, Y., and Esteban-Parra, M. J. (2015). Summer precipitation projections over northwestern south america from cmip5 models. *Global and Planetary Change*, 131:11–23.

Pérez, F. F., Boscolo, R., Blade, I., Cacho, I., Castro-Díez, Y., Gomis, D., Samperiz, G., Miguez-Macho, G., Rodríguez-Fonseca, B., Rodriguez-Puebla, C., et al. (2010). Clima en españa: pasado, presente y futuro. *Informe de Evaluacion del Cambio Climatico Regional*.

Preisendorfer, R. W. and Mobley, C. D. (1988). *Principal component analysis in meteorology and oceanography*. Elsevier Amsterdam.

Rasilla, D. F., Garmendia, C., and García-Codron, J. C. (2013). Climate change projections of streamflow in the iberian peninsula. *International Journal of Water Resources Development*, 29(2):184–200.

Riahi, K., Grübler, A., and Nakicenovic, N. (2007). Scenarios of long-term socioeconomic and environmental development under climate stabilization. *Technological Forecasting and Social Change*, 74(7):887–935.

Rodríguez-Puebla, C., Encinas, A., Nieto, S., and Garmendia, J. (1998). Spatial and temporal patterns of annual precipitation variability over the iberian peninsula. *International Journal of Climatology*, 18(3):299–316.

Rodríguez-Puebla, C. and Nieto, S. (2010). Trends of precipitation over the iberian peninsula and the north atlantic oscillation under climate change conditions. *International Journal of Climatology*, 30(12):1807–1815.

Rummukainen, M. (2010). State-of-the-art with regional climate models. *Wiley Interdisciplinary Reviews: Climate Change*, 1(1):82–96.

Sahriman, S., Djuraidah, A., and Wigena, A. H. (2014). Application of principal component regression with dummy variable in statistical downscaling to forecast rainfall. *Open Journal of Statistics*, 4(09):678.

Smith, S. J. and Wigley, T. (2006). Multi-gas forcing stabilization with minicam. *The Energy Journal*, pages 373–391.

Textor, C., Graf, H.-F., Herzog, M., and Oberhuber, J. (2003). Injection of gases into the stratosphere by explosive volcanic eruptions. *Journal of Geophysical Research: Atmospheres (1984–2012)*, 108(D19).

Timm, N. H. (2002). *Applied Multivariate Analysis*. Springer-Verlag, New York, NY, USA, 1st edition.

Trigo, R., Pozo-Vazquez, D., Osborn, T., Castro-Diez, Y., Gamiz-Fortis, S., and Esteban-Parra, M. (2004). North Atlantic oscillation influence on precipitation, river flow and water resources in the Iberian peninsula. *International Journal of Climatology*, 24(8):925–944.

Tullot, I. F. (2000). *Climatología de España y Portugal*, volume 76. Universidad de Salamanca.

Van Vuuren, D. P., Den Elzen, M. G., Lucas, P. L., Eickhout, B., Strengers, B. J., van Ruijven, B., Wonink, S., and van Houdt, R. (2007). Stabilizing greenhouse gas concentrations at low levels: an assessment of reduction strategies and costs. *Climatic Change*, 81(2):119–159.

Wayne, G. (2013). The beginner's guide to representative concentration pathways. *Available online at the following website: www. skepticalscience. com*.

Wigena, A. H. and Djuraidah, A. (2014). Quantile regression in statistical downscaling to estimate extreme monthly rainfall. *Science Journal of Applied Mathematics and Statistics*, 2(3):66–70.

Wilby, R. L., Wigley, T., Conway, D., Jones, P., Hewitson, B., Main, J., and Wilks, D. (1998). Statistical downscaling of general circulation model output: a comparison of methods. *Water Resources Research*, 34(11):2995–3008.

Wise, M., Calvin, K., Thomson, A., Clarke, L., Bond-Lamberty, B., Sands, R., Smith, S. J., Janetos, A., and Edmonds, J. (2009). Implications of limiting co2 concentrations for land use and energy. *Science*, 324(5931):1183–1186.

WMO (2012). *International Glossary of Hydrology, World Meteorological Organization. WMO-No. 385. ISBN 978-92-63-03385-8*.

Zorita, E. and Von Storch, H. (1999). The analog method as a simple statistical downscaling technique: comparison with more complicated methods. *Journal of climate*, 12(8):2474–2489.